

To the Graduate Council:

I am submitting herewith a dissertation written by Archil Garishvili entitled “Nuclear Modification Factor for Production of Open Heavy Flavor at Forward Rapidity in Cu+Cu Collisions”. I have examined the final paper copy of this dissertation for form and content and recommend that it be accepted in partial fulfillment of the requirements for the degree of Master of Science, with a major in Physics.

Kenneth F. Read, Major Professor

We have read this dissertation
and recommend its acceptance:

Soren P. Sorensen

Yuri Efremenko

Accepted for the Council:

Carolyn R. Hodges

Vice Provost and Dean of the Graduate School

(Original signatures are on file with official student records)

**Nuclear Modification Factor for
Production of Open Heavy Flavor
at Forward Rapidity in Cu+Cu
Collisions**

A THESIS
PRESENTED FOR THE
MASTER OF SCIENCE
DEGREE
THE UNIVERSITY OF TENNESSEE, KNOXVILLE

ARCHIL GARISHVILI
DECEMBER 2011

Dedicated to my family

Acknowledgements

First of all, I would like to thank my adviser Ken Read for all the support and help which I got from him during those years. I also would like to thank my adviser for very professional and meaningful corrections of my thesis. Without Ken I would not be where I am right now.

I am very grateful to head of Physics department Soren Sorensen. Thank you very much Soren for being in my defence committee, for corrections of my thesis, for all the physics discussions we went through, for all advises and directions, and also very big thank you for always being supportive to me. I also would like to thank Soren's wife Dianna for always being very nice to me, to my mom and to Andrea.

I am very thankful to Professor Yuri Efremenko, for being in my defence committee, for providing very proper corrections in my thesis, and also to give me chance to do some work related to VTX. Thank you very much Professor Yuri for all your help and support.

I would like to say huge “thank you” to Christine Nattrass. Since I know Christine, she always has been ready to help me in problems I had so far at UT. Besides being just excellent colleague, Christine has been always nice, supportive and helpful to me, I do not know that much words in English to describe how grateful I am to you Christine.

Also I would like to appreciate all the help I got from former RHIP graduate student Donny Hornback. Thank's a lot Donny for everything.

I am very grateful to current RHIP graduate students: Kyle Schmoll, Irakli Martashvili, Joel Mazer, and Rebecca Scott for always being very nice and helpful to me. Also I would like thank members of RHIP-ORNL group: Vince Cianciolo, Cheuk-Yin

Wong and Akitomo Enokizono for all the discussions about heavy ion physics, which really helped me to understand this field of physics.

Also I would like to say thank you to my classmates at UT: Savnan Kharel and Marwan Sahli. Thanks guys for being my excellent friends and for all the physics discussions we had.

Without my friends here in Knoxville, my life would not be as bright as it is right now. I would like to thank Mladen Grbovic, Vlado Pjesivac, Elody Vonachen, Ben Shultz and Winston for being great friends and make me feel here as at home.

Also I would like to thank my former colleague and friend Irakli Keshelashvili who is the reason why I am physicist. Thank's Irakli and Ketu for being always nice, friendly and very supportive to me.

As my brother told me once, we have the best family in the world, and I should say he is totally right. I want to thank my mom, Tiniko, my Brother Ika, my Sister-in-law Maria, my uncle Sasha, and my grandma Lena. All of you are just extraordinary people, I thank all of you for all the love and support, regardless how wrong or right I have been.

I am the luckiest guy in the world, because in Knoxville I met my fiancée Andrea Masi. Thank you Andrea for your love, care and support during this time.

Abstract

The PHENIX experiment at the Relativistic Heavy Ion Collider (RHIC) at Brookhaven National Laboratory with its muon spectrometer has the ability to detect muons over the range of pseudorapidity $1.1 < |\eta| < 2.25$. Single muon production is an important tool for studying heavy flavor production via semi-leptonic decays of open heavy flavor mesons. Because of their large mass, heavy quarks are produced in earlier stages of heavy ion collisions. Therefore, heavy flavor production can serve as an important probe of the Quark Gluon Plasma, a novel state of matter predicted to be created at RHIC. The measurement of the nuclear modification factor of open heavy flavor at forward rapidity in Cu+Cu collisions at $\sqrt{s_{NN}} = 200$ GeV is presented. Measurements of heavy flavor production in p+p collisions at $\sqrt{s_{NN}} = 200$ GeV will be also presented.

Contents

1	Introduction	1
1.1	Quark Gluon Plasma Physics	1
1.2	Theoretical Aspects of Relativistic Heavy Ion Collisions	5
1.2.1	Definition of Centrality	7
1.3	QGP at RHIC	8
1.4	Heavy Flavor Production in p+p Collisions	14
1.4.1	Single Muon Production	20
2	Experimental Setup	23
2.1	Relativistic Heavy Ion Collider	23
2.2	Setup of the PHENIX Experiment	26
2.3	PHENIX Muon Arms	29
2.3.1	Muon Tracker Sub-detector	29
2.3.2	Muon Identifier Sub-detector	32
2.4	Reconstruction of Tracks in the Muon Arms	35
2.5	Minimum Bias Trigger	36

2.6	PHENIX Dataflow	36
3	Single Muon Analysis	37
3.1	Overview	37
3.2	“Hadron Cocktail”	40
3.3	Signal Production	42
3.4	Acceptance and Efficiency Corrections	45
4	Background Monte Carlo Simulation	50
4.1	Overview of “Hadron Cocktail”	50
4.2	Initial Data Production	52
4.2.1	Variables in the Analysis	53
4.2.2	Non-hadron Cocktail Background	55
4.3	Matching of Data	56
4.4	Systematic Uncertainty	58
4.5	Single Muon Yield	62
4.6	Nuclear Modification Factor Calculations	62
5	Experimental Results	64
5.1	Single Muon Spectra	64
5.2	Cross Section Measurements	68
5.3	R_{AA} Measurements	71
6	Conclusions	74

6.1	Overview	74
6.2	Discussion	75
6.3	Comparisons	76
6.4	Future plans	77
	Bibliography	80
	Appendices	80
A	Weighted Sample Mean	82
A.1	R_{AA} Calculation Steps	83
A.2	Final Step	87
A.3	Simple Example	87
B	Charm Meson Decay Kinematics	89

List of Tables

2.1	RHIC runs for each year starting from 2000	25
4.1	Uncertainties in the acceptance and efficiency corrections	60
4.2	Uncertainties in the single muon analysis	61

List of Figures

1.1	$\alpha_s(\mu)$ vs. μ	3
1.2	QCD phase space diagram	4
1.3	The heavy ion collision in the frame of space-time diagram	6
1.4	Graphical view of the heavy ions collision.	8
1.5	Suppression of π^0 in Au+Au collisions observed by PHENIX	11
1.6	Correlated two-particle measurements by STAR	11
1.7	SPS measurements of charmonium suppression	13
1.8	Hadronization of the $c\bar{c}$	15
1.9	Heavy quark production described by LO Feynman diagrams	16
1.10	Fragmentation process of heavy quarks	17
1.11	Peterson and Lund modelsm fragmentation functions	18
1.12	Fermilab measurements of the invariant mass of D-meson	19
1.13	Non-photonic e^\pm yield of FONLL prediction.	21
2.1	The view of the RHIC	24
2.2	Scematic view of the PHENIX detector	26

2.3	Kinematic acceptance	27
2.4	South muon arm tracking detector.	30
2.5	Muon Tracking Nomenclature	31
2.6	Absorber materials in the south muon arm	33
2.7	Schematic view of Iarocci tubes	34
2.8	Schematic view of a MuID layer	34
3.1	Process of signal extraction	39
3.2	Normalized inclusive tracks in Gap 4	40
3.3	Longitudinal momentum of the tracks stopped in Gap 3	41
3.4	Acceptance \times efficiency corrections for North arm	46
3.5	Acceptance \times efficiency corrections for South arm	47
3.6	$A\epsilon_\mu$ correction factors vs. p_T	49
4.1	Variables for the analysis	54
4.2	Background via $p\delta\theta$ and δZ correlation	56
5.1	Single muon cross section	65
5.2	Cu+Cu and p+p invariant yields	67
5.3	Rapidity of charm production cross section in p+p	70
5.4	R_{AA} as a function of p_T for 0-20% centrality for combined arms . . .	72
5.5	R_{AA} as a function of p_T for 20-40% centrality for combined arms . . .	72
5.6	R_{AA} as a function of p_T for 40-94% centrality for combined arms . . .	73

6.1	R_{AA} vs. p_T for 0-20% centrality for combined arms compared with theoretical prediction	78
B.1	Momentum comparison	90
B.2	Rapidity comparison	92

Chapter 1

Introduction

It is a fact that the creation of our universe started with the “Big Bang”, which occurred 13.7 billion years ago. A very fundamental question is what did it look like? The answer is we still do not know. But based on our understanding, we know that 10^{-5} seconds after the “Big Bang” our universe consisted of a state of matter called the “Quark Gluon Plasma” (QGP). The Relativistic Heavy Ion Collider (RHIC) comes as a successor to create the QGP in laboratory conditions. This work is part of a huge scientific project whose main goal is to characterize the Quark Gluon Plasma.

1.1 Quark Gluon Plasma Physics

According to the Standard Model (SM), there are four fundamental forces: gravity, the weak force, the electromagnetic force and the strong force. The fermions are particles with half-odd intrinsic spin while the bosons are the particles with integer spin, some of which mediate the forces between fermions. Quarks and leptons are fermions, which come in three different families. Quarks are different from leptons

because they participate in strong interactions. Also, quarks can not exist as free particles. They occur in some specific combinations with other quarks, confined in particles called “hadrons”. There are two types of hadrons: baryons and mesons. Baryons consist of three quarks or three antiquarks, while mesons consist of a quark-antiquark pair.

The Quark Gluon Plasma is a state of matter in which quarks and gluons occur as free particles, under very high energy densities. In normal matter these particles are confined, while in the QGP they are deconfined. The strong interaction between quarks and gluons is described by the theory Quantum Chromodynamics (QCD). In QCD quarks are the fermionic components of mesons and baryons, while gluons are considered the bosonic components of such particles. The gluons are the carriers of the strong force, while the quarks by themselves are their fermionic matter counterparts. Quarks carry the strong (color) charge and interact between each other through gluons. This interaction is known as the strong interaction. In addition, since gluons carry color charge, they can interact with each other as well.

In order to quantify the strength of the strong interaction one should take into account the strong running coupling constant α_s [1], which can be described by Equation 1.1

$$\alpha_s(\mu) = \frac{2\pi}{b_0 \log(\mu/\Lambda_{QCD})} \quad (1.1)$$

where μ is the transferred momentum in the interaction, $b_0 = 11 - \frac{2}{3}n_f$ and n_f is the approximate number of massless quarks. The quantity Λ_{QCD} characterizes the momentum scale for which α_s becomes the “strong” coupling constant, which approximately equals 200 MeV. To be more accurate, α_s is not exactly the constant, since it varies with the transferred energy within an interaction.

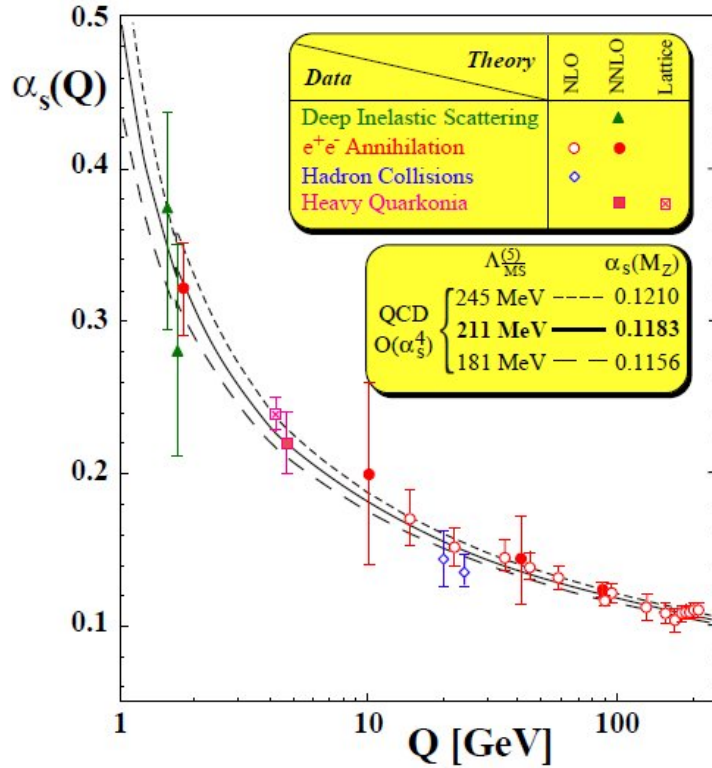


Figure 1.1: Comparison between the theoretical and the experimental running coupling constant of the strong interaction as a function of energy scale [2].

Figure 1.1 demonstrates the asymptotic freedom postulate [3] [4], which states that the effective coupling in interaction between quarks is infinitely strong for the energy range below Λ_{QCD} , whose inverse is about the same as the radius of hadrons (radius of hadron $\sim 1/\Lambda_{QCD} \sim 1$ fm). This postulate is also known as the “confinement”. However, for the bigger energies, the interaction becomes weaker and once the energy reaches the extreme limit $Q \gg \Lambda_{QCD}$, quarks are completely deconfined from hadrons. Also from Figure 1.1, we can clearly see that the theoretical predictions and the experimental measurements of the running coupling constant of the strong interaction agree well. If the energy density ϵ_c exceeds 1 GeV/fm^3 , nuclear matter undergoes a phase transition to a state of matter in which quarks and gluons are not bound inside the hadrons anymore, and become the appropriate effective degrees of freedom. This state of matter is called the Quark Gluon Plasma (QGP) [5]. It

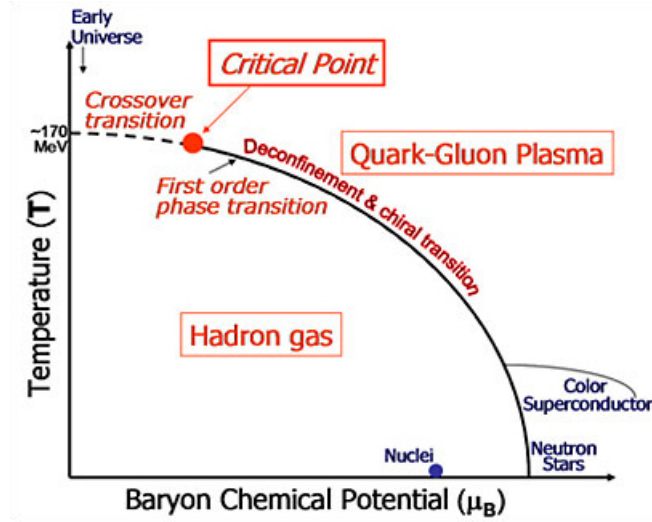


Figure 1.2: Phase space diagram of the QCD matter [6].

is believed that right after the "Big Bang", our universe was some kind of deconfined matter at very high temperature without existence of baryons. Additionally Figure 1.2 indicates that deconfined matter is predicted to exist at low temperatures in neutron stars. The critical temperature of the phase transition is predicted to be 170 MeV.

1.2 Theoretical Aspects of Relativistic Heavy Ion Collisions

In order to create the Quark Gluon Plasma, we need to create a system where the energy density ϵ_c , exceeds 1 GeV/fm^3 . This kind of system is possible to produce if one collides heavy nuclei at ultrarelativistic center of mass energies which are about 100 times greater than the rest mass of nuclei. These types of nucleon-nucleon collisions indeed produce novel nuclear matter which can be studied experimentally concerning its important properties, including its thermodynamic properties.

Figure 1.3 shows that there are several steps in colliding heavy ion system dynamics. At the very beginning of the collision, there are two incoming “Lorentz contracted” nuclei. The crossing time τ_{cross} of those nuclei is $2R/\gamma c \sim 0.1 \text{ fm/c}$. However, this crossing time is small compared to the time scale of the strong interaction, τ_{cross} , which is about $1/\Lambda_{QCD} \sim 1.0 \text{ fm/c}$. The nuclei pass through each other very rapidly and produce matter with very large energy density. Once this matter is created in the time range $\tau_{form} \leq 1 \text{ fm/c}$, the process of initial parton production begins. At $t = \tau_{therm}$, the strong interaction between partons leads the system to thermal equilibrium in 1 fm/c . During the expansion of the system, the energy density keeps dropping until it reaches the confinement limit where the system is completely hadronized and becomes a gas of hadrons which interact with each other. The last step of this process is when temperature reaches a critical temperature, where hadrons stop interacting with each other and will continue to fly towards detectors.

Once this complex process happened, the important issue is whether the energy density produced at formation time was large enough to create Quark Gluon Plasma. In order to say whether it was large enough or not, one should estimate the energy and the volume of the initial collision cross section, which is possible by backward extrapolation of the experimentally measured particle multiplicity of a collision.

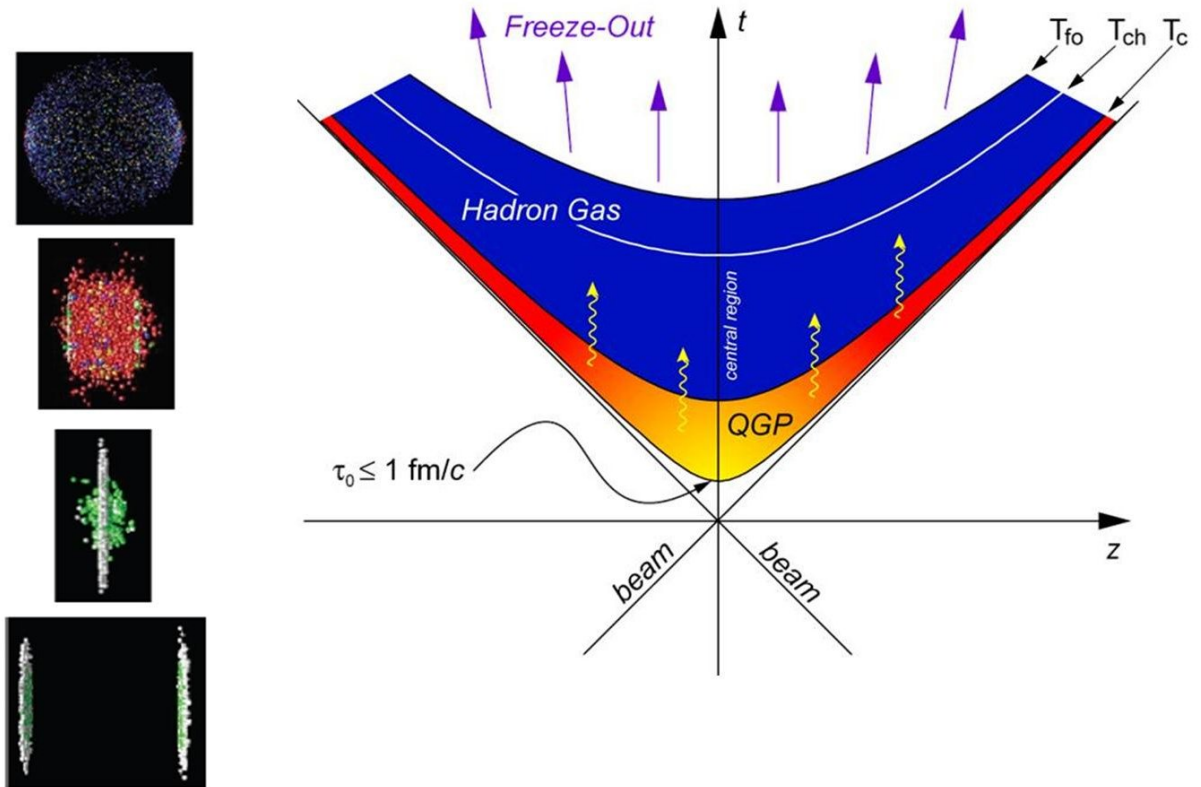


Figure 1.3: Heavy ion collision space-time diagram (right), stages of the collision dynamics (left) [6].

For the energy density calculations, Bjorken's formula [7] applies:

$$\epsilon_0 = \frac{\langle m_T \rangle}{\tau_0 A_T} \frac{dN}{dy} \Big|_{z=0} \quad (1.2)$$

where τ_0 is the formation time (≈ 1 fm/c), $\langle m_T \rangle$ is the average transverse mass per produced particle, which is measured experimentally, A_T is the effective transverse overlap area of the ions participating in the collisions, and $\frac{dN}{dy}$ is the particle multiplicity.

Using Bjorken's formula and by analyzing experimental data, the energy density of the matter created in head-on Au+Au collisions at RHIC is at least 15 GeV/fm³ [8]. Also, the time interval for the thermalization of the matter is quite short, about 0.6 to 1 fm/c. The energy density of this matter is in the range of 5.7 to 9.5 GeV/fm³, which is much higher than the predicted threshold energy density for the creation of a Quark Gluon Plasma.

1.2.1 Definition of Centrality

For different center of mass collision energies and for different species of colliding ions, heavy ion collisions can have various energy densities and hadron multiplicities. These differences depend on the so-called impact parameter b , which is the initial overlap of the incoming nuclei participating in a collision (Figure 1.4(a)).

Knowing the impact parameter, one can estimate the number of nucleons, N_{part} , participating in the heavy ion collision. Generally, each nucleon collides with other participating nucleon many times, i.e. the number of binary inelastic nucleon-nucleon collisions, N_{coll} , is obviously always bigger than N_{part} for heavy ion collisions. Depending on the b , N_{coll} , and N_{part} parameters, heavy ion collisions can be classified by collision centrality. The range for the impact parameter is $0 < b < 2R$, where R

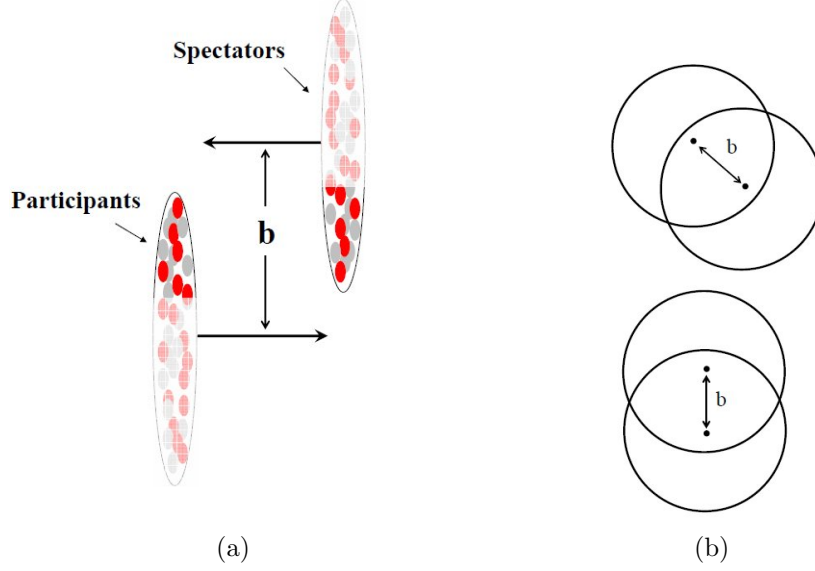


Figure 1.4: (a) Illustration of a “Lorentz contracted” heavy ions collision. (b) The overlap between the colliding nuclei, for impact parameter b [6].

is the radius of nuclei.

It is impossible to perform direct measurements of the impact parameter at RHIC. In order to calculate the impact parameter, the number of the nucleon-nucleon collisions and the number of the participant nucleons, one should combine the experimentally measured particle multiplicity with the Glauber model [9] Monte Carlo simulation of the heavy ion collision. Based on results, we define several classes of centrality and report it in percentage. For example in our analysis, 0% - 20% centrality corresponds to the most central collisions.

1.3 QGP at RHIC

The Quark Gluon Plasma is a partonic state of matter which has a very short lifetime. Because of the short lifetime, it is impossible to observe the QGP directly. The main goal of the heavy ion physics at RHIC is to perform experimental measurements of

the hadron observables with clear theoretical interpretations and characterize the created state of matter in heavy ion collisions. Those theoretical interpretations tested by experimental results could significantly improve understanding of this state of matter. Since the very first collisions at RHIC, huge progress has been made through successful studies related to the very early period of our universe.

Jet quenching is a phenomenon that can occur in the collision of high energy particles. In general, the collision of high energy particles can produce jets of elementary particles that emerge from these collisions. Collisions of relativistic heavy ion particle beams create a hot and dense medium comparable to the conditions in the early universe, and then these jets interact strongly with the medium, leading to a marked reduction of their energy. This energy reduction is called “jet quenching”.

In the context of high energy hadron collisions, quarks and gluons are collectively called partons. The jets emerging from the collisions initially consist of partons, which quickly combine to form hadrons, a process called hadronization. Only the resulting hadrons can be directly observed. The hot, dense medium produced in the collisions is also composed of partons and constitutes the QGP. In this realm, the laws of physics that apply are those of QCD.

High energy nucleus-nucleus collisions enable the study of the properties of the QGP medium through observed changes in jet fragmentation functions as compared to the unquenched case. According to QCD, high momentum partons produced in the initial stage of a nucleus-nucleus collision will undergo multiple interactions inside the collision region prior to hadronization. In these interactions, the energy of the partons is reduced through collisional energy loss and medium induced gluon radiation. The effect of jet quenching in a QGP is the main motivation for studying jets as well as high-momentum particle spectra and particle correlations in heavy ion collisions. Accurate jet reconstruction will allow measurements of the jet fragmentation functions, and consequently the degree of quenching, and provide insight into the

properties of the hot dense QGP medium created in the collisions. First evidence of parton energy loss has been observed at RHIC from the suppression of high p_T particles manifested by the nuclear modification factor and the suppression of back to back correlations [10],[11].

In heavy ion collisions, medium effects can be quantified via a quantity called nuclear modification factor:

$$R_{AA} = \frac{dN_{AA}}{\langle N_{coll} \rangle dN_{p+p}} \quad (1.3)$$

where dN_{AA} is invariant yield of the measured hadron production from the jet fragmentation in A+A collisions and dN_{p+p} is invariant yield of measured hadron production from the jet fragmentation in p+p collisions. If $R_{AA} < 1$, it means that observed yield is suppressed for A+A collisions compared to naively scaled expectations in p+p collisions. If $R_{AA} > 1$, it means that the observed yield is enhanced.

From Figure 1.5 we observe large suppression of high p_T hadron production for central Au+Au collisions. Those measurements have been done by the PHENIX Collaboration. Separate measurements by the STAR Collaboration (Figure 1.6) show complete disappearance of the high p_T components of away-side jets in central Au+Au collisions, while for p+p and d+Au we can observe a clear peak.

The only possible explanation of those effects could be the presence of a strongly interacting and very dense medium.

Another big goal of the heavy ion physics program at RHIC is to study charmonium suppression, which may support that the very dense matter created in heavy ion collisions is deconfined.

The bound state of the charm anti-charm (c and \bar{c}) quark pairs form the charmonium vector meson. The most stable charmonium vector meson is J/ψ particle, which

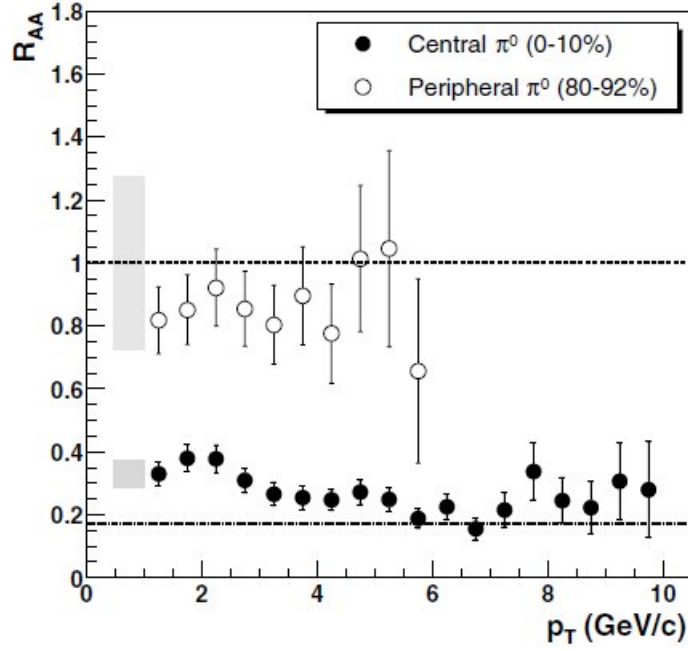


Figure 1.5: The nuclear modification factor for π^0 in Au+Au collisions for the very central collision. Measurements performed by PHENIX [10].

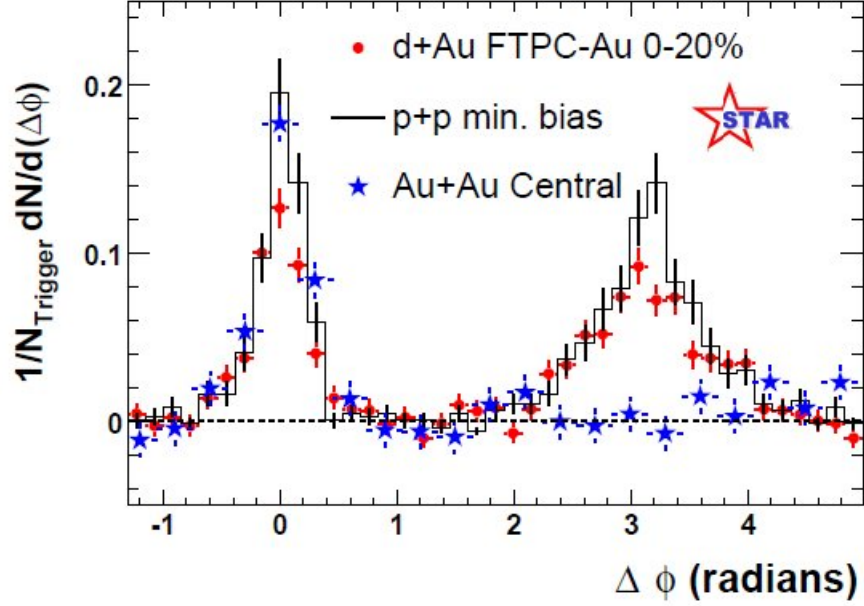


Figure 1.6: The distribution of the correlated two-particle azimuthal in very central Au+Au, p+p and d+Au collisions. Measurements performed by the STAR experiment [11].

results from the hadronization of c and \bar{c} quarks produced in the collision. The confining potential between c and \bar{c} at long distances varies as

$$V_0(r) \sim \sigma r, \quad (1.4)$$

where σ is the string tension and r is distance between the quarks [12]. From this relation we can conclude that a large amount of energy is required to break the bound state of the charm anti-charm pair. But in very dense matter, the confining potential depends on the other "color" charges and varies as:

$$V_0(r) \sim \sigma r \left[\frac{1 - e^{-\mu r}}{\mu r} \right] \quad (1.5)$$

where μ is inverse of the screening radius [13]. In the other words, production of J/ψ particles should be suppressed in deconfined matter. Measurements from the SPS at CERN [14] (Figure 1.7) exhibit suppression for central collisions, while there is no suppression for peripheral collisions. This was regarded as a potential signal of the creation of the Quark Gluon Plasma.

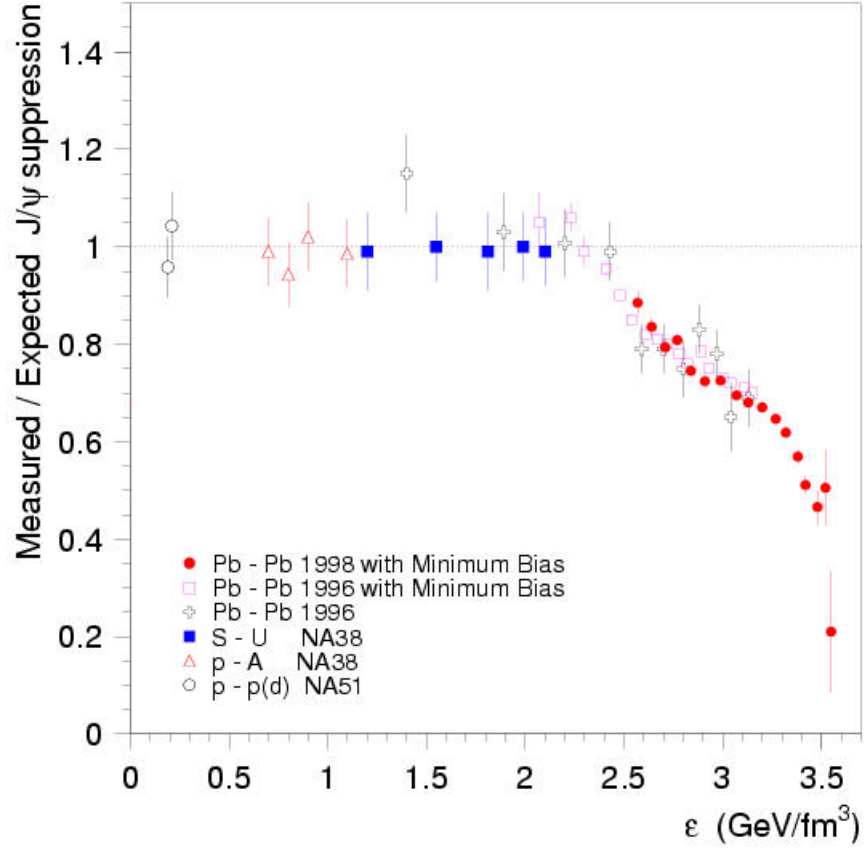


Figure 1.7: The charmonium production measurement of the different ion species at SPS [14].

Those results and also other observations at RHIC tend to support strongly interacting and very dense matter produced in heavy ion collisions is deconfined.

1.4 Heavy Flavor Production in p+p Collisions

In heavy ion collisions at RHIC, the produced very dense deconfined matter consists of gluons and mostly light quarks. There is only a small fraction of the heavy quarks produced at RHIC center of mass energies. The production of heavy flavor in p+p collisions is an important baseline for studying the heavy quarks in heavy ion collisions. Heavy flavor production in p+p collisions also can be used to test QCD at large center of mass energies. In heavy ion collisions depending on the mass of the heavy quarks, they are produced before the creation of deconfined matter. Those “early” quarks can be used as a probe of the matter created earlier. Because of their interaction with the medium, their kinematics is modified, which is followed by the modification of the heavy flavor hadron spectra. Better understanding of those processes could lead to understanding the modification of the charmonium production in heavy ion collisions. So for this reason the measurements of charm anti-charm pairs have great importance.

In order to understand the mechanism of the production of heavy quarks in heavy ion collisions, first we should understand the mechanism of heavy flavor production in p+p collisions. Within the QCD framework, heavy flavor production is well enough understood due to the past experimental observations, but there are still remain important issues which should be determined.

Figure 1.8 represents the process of heavy flavor production in the hard p+p collisions. Once the heavy quarks are created they hadronize into heavy flavor hadrons, which afterward decay into other particles. Those product particles later can be experimentally detected.

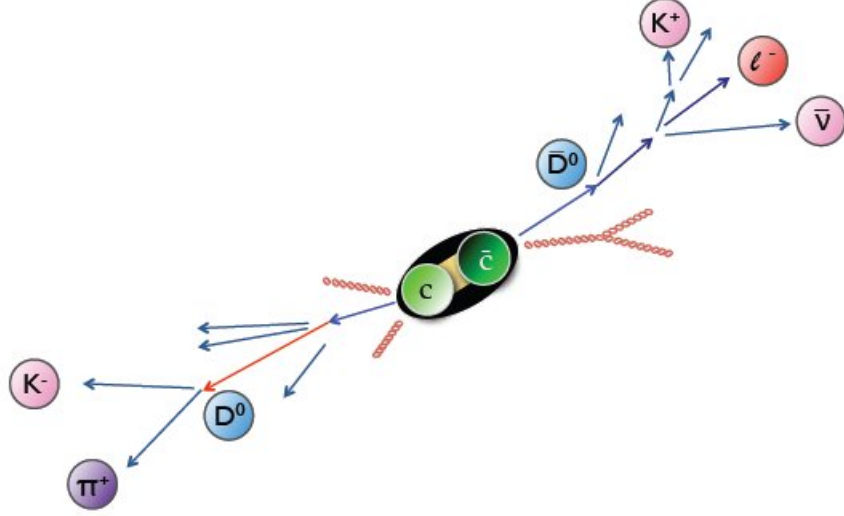


Figure 1.8: Hadronization process of the created $c\bar{c}$ -pair [15].

Factorization theorem

The *factorization theorem* framework [16], is used to theoretically describe the hadron collisions in which the initial hard parton collisions produce the initial heavy quarks. From the factorization theorem, the inelastic cross section for the production of heavy quark Q produced in the collision of A and B is calculated by:

$$E \frac{d\sigma_{AB \rightarrow Q}}{d^3p} = f_{i/A}(x, \mu) \otimes f_{j/B}(x, \mu) \otimes E \frac{d^3\hat{\sigma}_{ij}(s)}{d^3p} \quad (1.6)$$

where $f_{i/A}(x, \mu)$ is the probability distribution function for i -th gluon, light quark or anti-quark inside hadron A for a given energy scale μ and momentum fraction x of hadron A carried by the i -th parton, $f_{j/B}(x, \mu)$ is the probability distribution function for j -th gluon, light quark or anti-quark inside hadron B for a given energy scale μ and the momentum fraction x of hadron B carried by the j -th parton and $\hat{\sigma}_{ij}(s)$ is the cross-section of heavy quark production in the collision between i -th and j -th partons, with \otimes indicating a generic convolution.

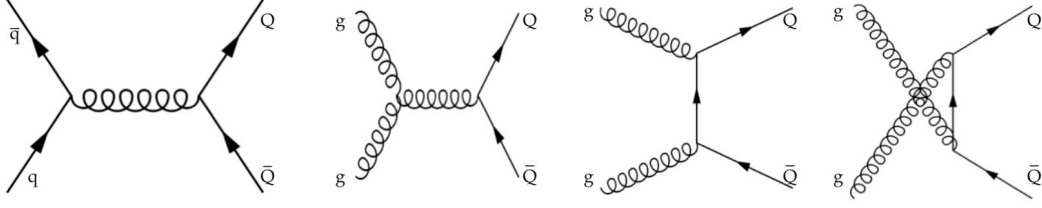


Figure 1.9: Leading order Feynman diagrams for the creation of heavy quark pairs: *quark anti-quark annihilation* (far left) and three different kinematic channels of *gluon-gluon fusion*[6].

In the context of the factorization theorem, point-like interactions of partons (not hadrons) lead to the production of heavy quarks in hadronic collisions. Partonic interactions with the specific hadron collision kinematics are dependent on the probability distribution functions.

Since the energy range ($\mu \sim 2m_Q$) of heavy quark creation is larger than the QCD scale Λ_{QCD} , the running coupling constant, $\alpha_s(Q)$, is small. This means that the cross-section $\hat{\sigma}_{ij}$ can be calculated as a perturbation series in α_s and the leading terms in perturbation series can be written as $\mathcal{O}(\alpha_s^2)$. Figure 1.9 shows the leading order process for the heavy quark production $q\bar{q} \rightarrow Q\bar{Q}$ and $gg \rightarrow Q\bar{Q}$. But at RHIC, gluon-gluon fusion is predicted to be the dominant contribution for heavy flavor production. Since the densities of anti-partons are very small compared to the densities of gluons inside the proton, quark anti-quark annihilation can be neglected.

Recent measurements have demonstrated that it is important for the Next-to-Leading Order (NLO) of $\mathcal{O}(\alpha_s^3)$ contribution to be included in the calculations.

Fragmentation

Creation of the heavy quarks is followed followed by hadronization, during which the produced heavy quarks become heavy hadrons. Less frequently the created pair of heavy quarks forms a *heavy quarkonium* meson, where charmonium is the bound

state of $c\bar{c}$ (and bottomonium is the bound state of $b\bar{b}$).

In more than 99% of cases, the produced heavy quarks bind with light quarks to form “open” heavy flavor mesons. The example of open heavy flavor mesons are: D mesons which are a combination of $c\bar{q}$ or $\bar{c}q$ and B mesons, which are a combination of $b\bar{q}$ or $\bar{b}q$. D mesons are often referred to open charm mesons, while B mesons are called open bottom mesons.

Figure 1.10 indicates process of fragmentation. The mechanism of the fragmentation process is not completely understood. There is a momentum degradation of the heavy quark resulting from the combination of the heavy quark with the light quark. The momentum degradation can be described by the fragmentation function $D_Q^H(z)$, which estimates the energy distribution of the formed hadron (E_H) with respect to the energy of the heavy quark (E_Q), where $z = E_H/E_Q$.

The fragmentation functions are universal functions because the fragmentation process is independent of the process in which the quark was produced. The qualitative description of the hadronization light quarks is parametrized by $D_Q^h(z) \propto \frac{(1-z)^n}{z}$ [17].

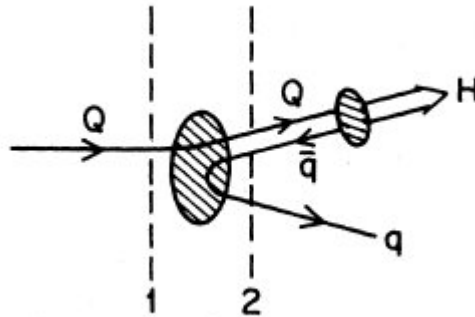


Figure 1.10: Possible heavy quark fragmentation process into heavy flavor meson [18].

During the hadronization process, heavy quarks keep the dominant part of their

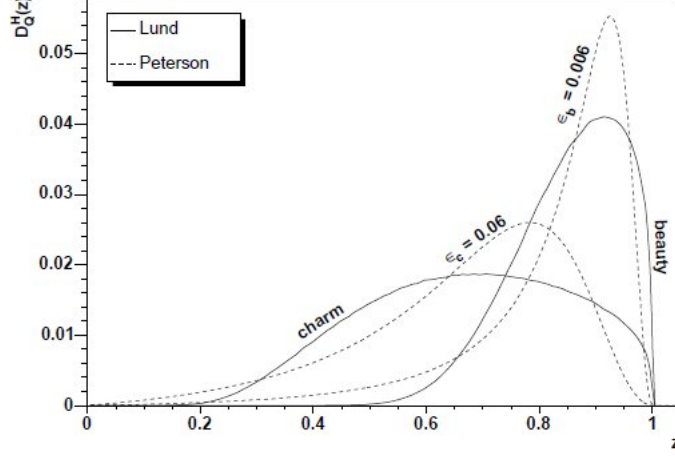


Figure 1.11: Heavy quarks fragmentation functions: The parametrization from Peterson et al. [18] (dashed lines) and the Lund string model parametrization [19] (solid lines).

momenta. The $D_Q^H(z)$ distribution for heavy quarks has a peak near $z = 1$ [17], as shown in Figure 1.11. The dashed lines represent the fragmentation functions introduced by Peterson et al. [18] parametrized as

$$D_Q^H(z) \propto \frac{1}{z[1 - (1/z) - \epsilon_Q/(1-z)]^2} \quad (1.7)$$

with the parameter ϵ_Q , originally introduced as $\epsilon_Q = (m_q/m_Q)^2$, fixed at 0.06 for charm and 0.006 for bottom. This function has a maximum at $z \approx 1 - \sqrt{\epsilon_Q}$. The solid lines, corresponding to a harder fragmentation scheme, represent the predictions based on the Lund string model [19] parametrized as

$$D_Q^H(z) \propto \frac{(1-z)^a}{z^{1+bm_Q}} e^{-\frac{bm_Q^2}{z}} \quad (1.8)$$

with $a = 0.3$, $b = 0.58 \text{ GeV}^{-2}$, $m_c = 1.5 \text{ GeV}/c^2$ and $m_b = 4.8 \text{ GeV}/c^2$.

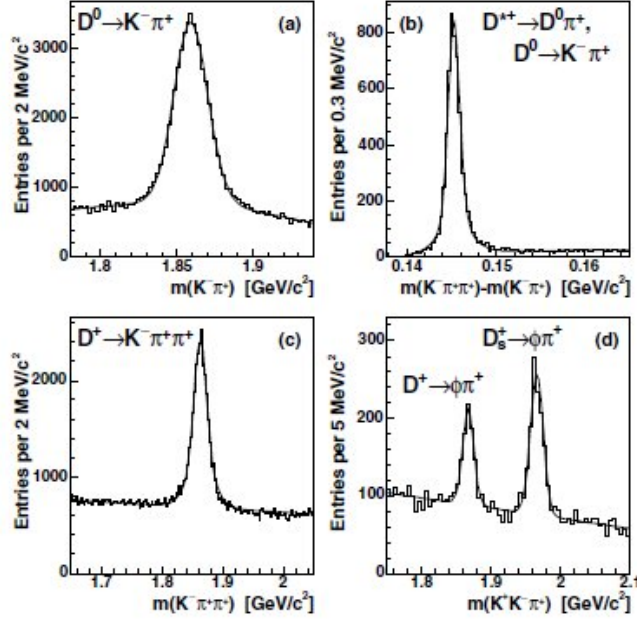


Figure 1.12: The invariant mass of D-mesons measured in $p\bar{p}$ collisions at $\sqrt{s} = 1.92$ TeV by CDF [20].

Decay

Because of their short lifetime, heavy flavor mesons can only be detected via their daughter particles. Heavy flavor mesons decay into multiple decay channels. The *branching ratio* is the experimentally measurable value which determines the probability of the each channel decay. There are two classes of decay modes of open heavy flavor mesons: *hadronic decays* and *semi-leptonic decays*. An example of hadronic decay is indicated on the left side of Figure 1.8, where the D^0 meson decays into $K^- \pi^+$. For this particular channel, the measured invariant mass distribution of the daughter particles K^- and π^+ is shown in Figure 1.12 (upper left).

For the case of semileptonic decay of open heavy flavor (the right side of Figure 1.8), it is impossible to reconstruct all the daughter particles. From those daughter particles, in some experiments only the lepton can be measured experimentally. Later, this “single” lepton is used for tagging the D^0 meson, which serves as an indirect

measurement of open heavy flavor.

In studying the production of open heavy flavor via semileptonic channels, all the detected lepton sources have to be identified carefully with backgrounds later subtracted from the entire lepton yield. In addition, the predictions from theoretical models must be foreseen, since the transverse momentum distribution of the resulting lepton yield will be different from the original transverse momentum distribution due to semileptonic decay mode kinematics. Theoretical aspects and several experimental results can be found in [21], [22] and [23].

1.4.1 Single Muon Production

The theoretical models which predict the single lepton production in p+p collisions consist of three ingredients describing the process of heavy flavor production:

- The invariant cross section of heavy quarks should be calculated in the pQCD framework.
- Fragmentation functions should be derived by the comparison of a dedicated fragmentation model with e^+e^- data.
- Final lepton yields should be calculated from semileptonic decays of heavy flavor mesons.

The invariant cross section of the lepton production can be described as:

$$E \frac{d^3\sigma(l)}{d^3p} = E_Q \frac{d^3\sigma(Q)}{d^3p_Q} \otimes D(Q \rightarrow H_Q) \otimes f(H_Q \rightarrow l) \quad (1.9)$$

where $E_Q \frac{d^3\sigma(Q)}{d^3p_Q}$ is the heavy quark production invariant cross section, calculated from the factorization theorem, $D(Q \rightarrow H_Q)$ is heavy quark fragmentation function

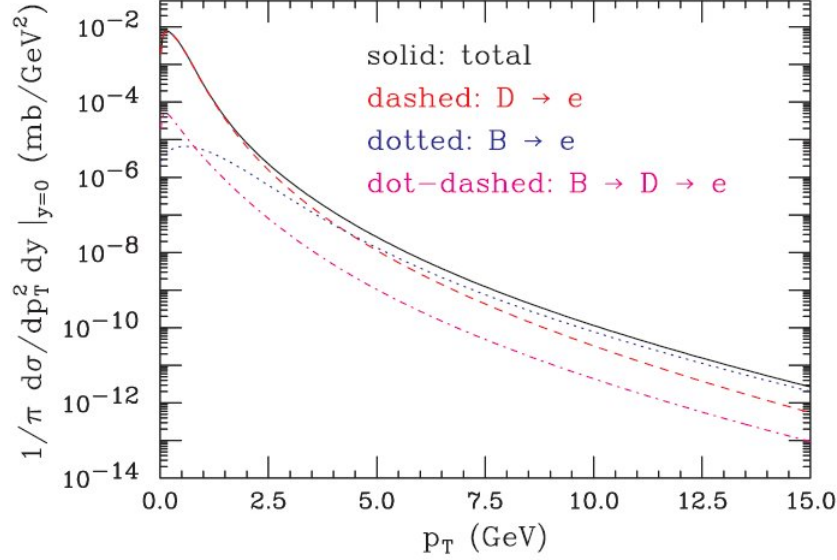


Figure 1.13: The FONLL prediction of the invariant cross section of non-photonic e^\pm 's, which are the products of the semileptonic decays of heavy flavor mesons. At $p_T < 5$ GeV/c the spectra is dominated by heavy flavor electrons from $D \rightarrow e$. At $p_T \geq 5.0$ GeV/c electrons are mainly produced from $B \rightarrow e$ [24].

and $f(H_Q \rightarrow l)$ is the single lepton yield calculated from the heavy flavor meson decays.

FONLL [24], an acronym for of “Fixed-Order(FO) plus Next-to-Leading-Log(NLL)”, is the most advanced theoretical framework for predicting heavy flavor production by incorporating the scheme described by Equation 1.9. Within the FONLL framework, the heavy quark production cross section, $E_Q \frac{d^3\sigma(Q)}{d^3p_Q}$, is calculated by including the standard fixed-order NLO results and the finalization of large perturbative terms proportional to $\alpha_s^n \log^k(p_T/m)$ arising from renormalization/factorization scale dependence [25], especially at high p_T . The fragmentation functions for the charm and bottom quarks, $D(c \rightarrow D)$ and $D(c \rightarrow B)$, used with the FONLL scheme are extracted from the e^+e^- data using the parametrizations from [26] and [27].

For predicting the total single lepton yield from the decays of heavy flavor mesons, the individual lepton yields produced from $D \rightarrow l$, $B \rightarrow l$ and $B \rightarrow D \rightarrow l$ decays

are combined. Those are extracted from BABAR and CLEO data, [28] [29]. Later, single lepton yields are normalized by using corresponding branching ratios from [30] and the chemistry of the production of D and B mesons.

Chapter 2

Experimental Setup

2.1 Relativistic Heavy Ion Collider

The Relativistic Heavy Ion Collider (RHIC) is the first collider built and designed for the ultra-relativistic heavy ion collisions. RHIC is located at the Brookhaven National Laboratory (BNL) on Long Island, NY.

Figure 2.1 shows a schematic view of RHIC. The circumference of RHIC is about 3.8 km. The ring includes two separate beamlines, each of those beamlines equipped with a series of the superconducting magnets. The injected ion beam is accelerated almost up to the speed of light. The entire pre-injection process of the beam is described in [15].

Two beamlines cross each other at six different points, where the actual collisions can occur. Figure 2.1 shows the location of the four RHIC experiments: BRAHMS, PHENIX, PHOBOS and STAR. Each of those experiments is located at a different beamline crossing point.

RHIC has the ability to accelerate various heavy ion beams up to 100 GeV per nucleon energy, allowing experiments at center of mass energy $\sqrt{s_{NN}} = 200$ GeV per nucleon-nucleon collision. As a remarkable exception, one should mention that in 2009, RHIC reached a center of mass energy for p+p collisions of $\sqrt{s_{NN}} = 500$ GeV.

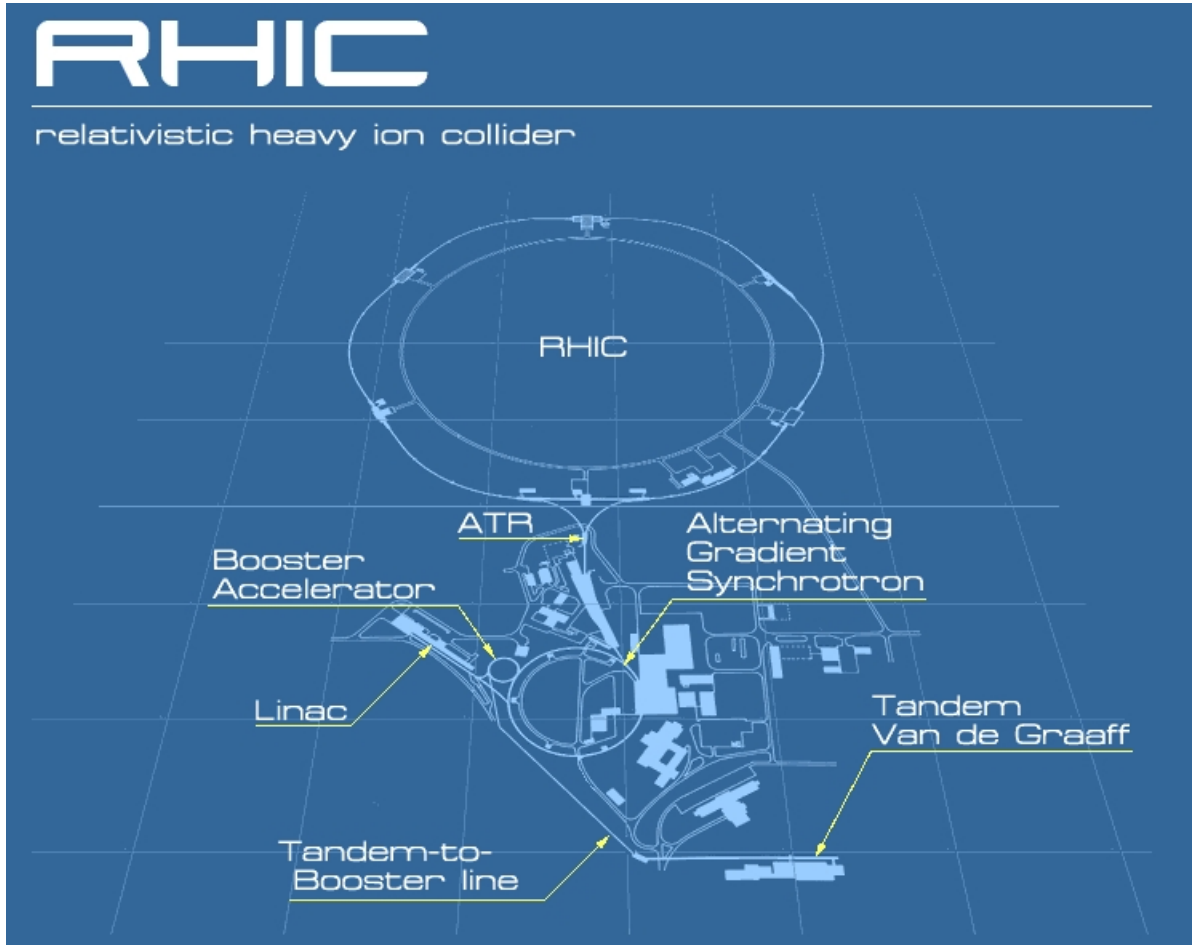


Figure 2.1: The RHIC complex.

Starting from the very first collisions in 2000, collisions of different nuclei species at various center of mass energies have been delivered at RHIC. Table 2.1 illustrates the main parameters for each run at RHIC starting from 2000. The data used for the analysis presented in this thesis were taken in 2005 during Run 5, specifically p+p and Cu+Cu collisions at 200 GeV center of mass energy per nucleon-nucleon pair.

Table 2.1: Collision species, center of mass energy, luminosity achieved by PHENIX, total number of events, and the total size of data for RHIC runs since 2000.

	Year	Species	\sqrt{s} [GeV]	$\int \mathcal{L} dt$	$N_{tot(sampled)}$	Data Size
Run-1	2000	Au+Au	130	$20 \mu b^{-1}$	10 M	3 TB
Run-2	2001/02	Au+Au	200	$258 \mu b^{-1}$	170 M	10 TB
		p+p	200	$1.4 pb^{-1}$	3.7 B	20 TB
		Au+Au	19		1 M	
Run-3	2002/03	d+Au	200	$73 nb^{-1}$	5.5 B	46 TB
		p+p	200	$5.5 pb^{-1}$	6.6 B	35 TB
Run-4	2003/04	Au+Au	200	$3.53 \mu b^{-1}$	1.5 B	
		Au+Au	62.4	$67 \mu b^{-1}$	58 B	10 TB
		p+p	200	$5.5 pb^{-1}$		
Run-5	2004/05	Cu+Cu	200	$42.1 nb^{-1}$	170 M	173 TB
		Cu+Cu	62.4	$1.5 nb^{-1}$	3.7 B	48 TB
		Cu+Cu	22.4	$0.02 nb^{-1}$	3.7 B	1 TB
		p+p	200	$29.5 pb^{-1}$	85 B	262 TB
		p+p	409.8	$0.1 pb^{-1}$		
Run-6	2006	p+p	200	$88.6 pb^{-1}$	233 B	310 TB
		p+p	62.4	$1.05 pb^{-1}$	10 B	25 TB
Run-7	2007	Au+Au	200	$7.25 nb^{-1}$	4.6 B	570 TB
		Au+Au	9.2	small	few K	
Run-8	2007/08	d+Au	200	$437 nb^{-1}$	160 B	437 TB
		p+p	200	$38.4 pb^{-1}$	115 B	140 TB
		Au+Au	9.2	small	few K	
Run-9	2008/09	p+p	500	$110 nb^{-1}$	308 B	
		p+p	200	$114 pb^{-1}$	936 B	
Run-10	2009/10	Au+Au	200	$10.3 nb^{-1}$	8.2 G	
		Au+Au	62.4	$544 \mu b^{-1}$	700 M	
		Au+Au	39	$206 \mu b^{-1}$	250 M	
		Au+Au	7.7	$4.23 \mu b^{-1}$	1.6 M	
		Au+Au	11.5	$7.8 \mu b^{-1}$		
Run-11	2010/11	p+p	500	$166 pb^{-1}$		
		Au+Au	19.6	$33.2 \mu b^{-1}$		
		Au+Au	39	$206 \mu b^{-1}$		
		Au+Au	27	$63.1 \mu b^{-1}$		

2.2 Setup of the PHENIX Experiment

The PHENIX (**P**ioneering **H**igh **E**nergy Nuclear Interaction **eX**periment) [31] Experiment was built in order to study the properties of the matter produced in the heavy ion collisions. It is one of the leading large physics experiments in the world.

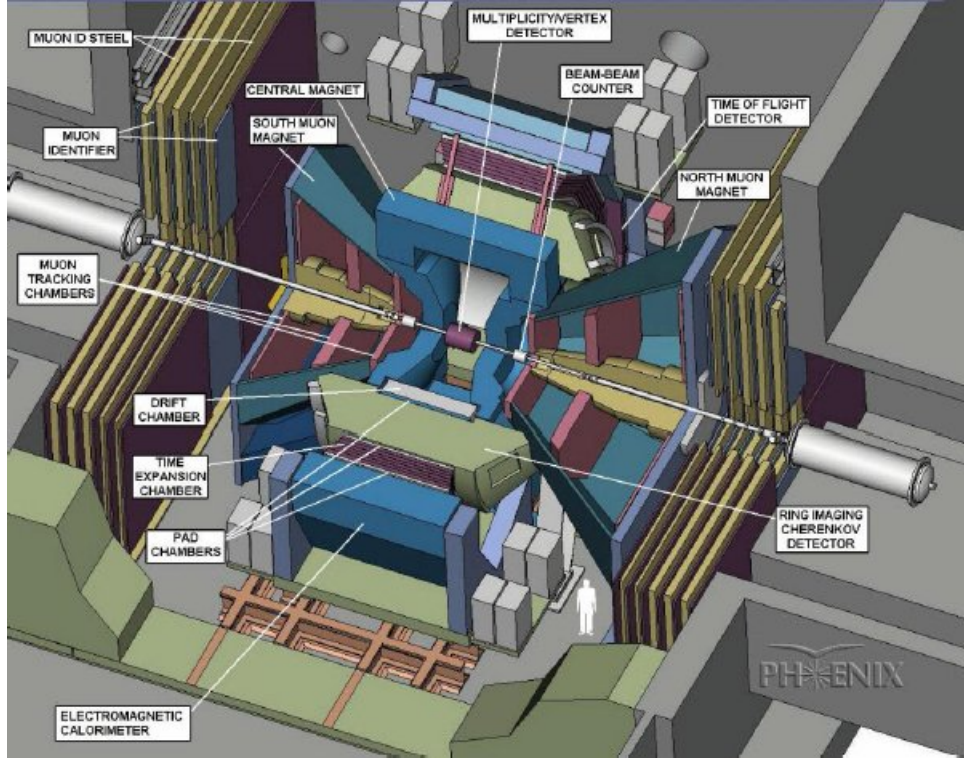


Figure 2.2: Schematic view of the PHENIX detector.

A schematic picture of the PHENIX detector is presented in Figure 2.2. The PHENIX coordinate system is designed such that the interaction point of the beamlines serves as the origin of the PHENIX coordinate system. In this coordinate system, the z -axis for the Cartesian and cylindrical coordinate systems lies along the beamline, where the positive direction is from South to North, which is from left to right in Figure 2.2. The kinematic acceptance of the PHENIX detector is presented in Figure 2.3.

The PHENIX detector consists of three main parts. The first main part of the detector is composed of two subdetectors: the Beam-Beam Counter (BBC) and

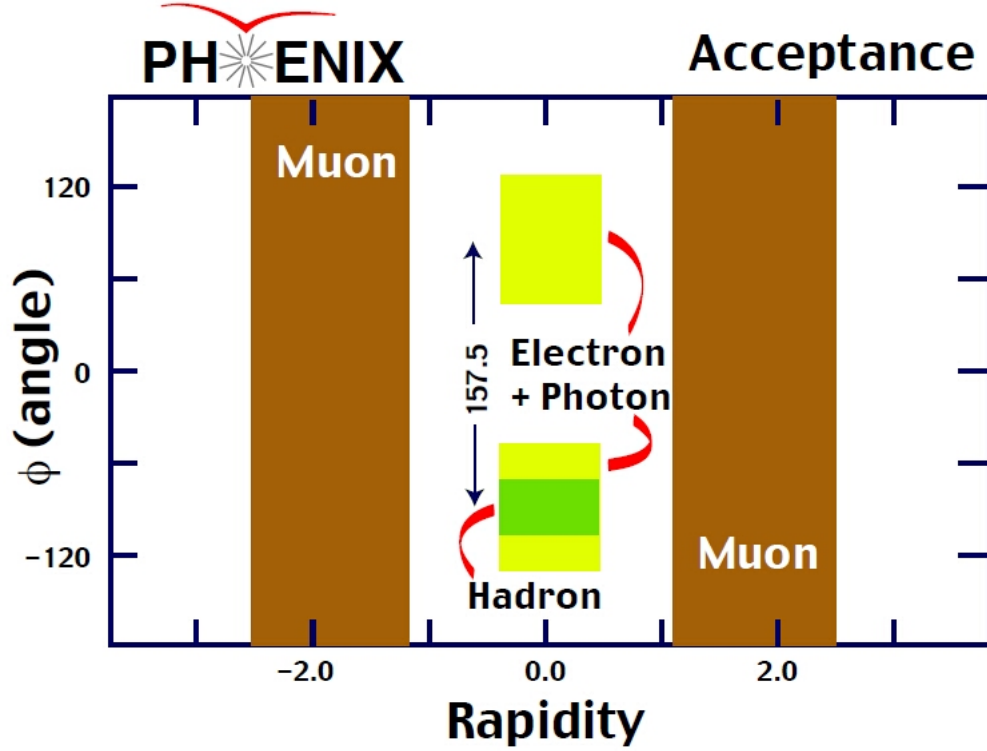


Figure 2.3: The kinematic acceptance range of the PHENIX detector.

Zero Degree Calorimeter (ZDC). BBC is responsible for measurements of the global event characteristics, for instance determination of the centrality and measurements of the z-coordinate of the collision vertex. Also, the BBC provides the selection for minimum bias triggered events. The ZDC is used for triggering and centrality determination. As of RHIC Run 5, ZDC operation was minimal.

The second main part of the detector is two “central arms” equipped with multiple subsystems such as: Pad Chambers (PC), Drift Chambers (DC), Ring-Imaging Cherenkov Detectors (RICH), Time Expansion Chamber (TEC), ElectroMagnetic Calorimeter (EMCal), and a Time-Of-Flight detector (TOF). The total kinematic coverage of both “central arms” is π in azimuth and $|\eta| \leq 0.35$ in pseudorapidity, which is defined as:

$$\eta = \frac{1}{2} \ln \left(\frac{p + p_z}{p - p_z} \right), \quad (2.1)$$

where p is the total momentum defined as $p \equiv |\vec{p}| = (p_x, p_y, p_z)$ and p_z is the momentum along the z-axis. In this kinematic range it is possible to provide measurements of electrons, charged hadrons, and photons.

The third main part of the PHENIX detector is two muon spectrometers, called the North and South muon arms. Both muon arms are designed to measure muon tracks within $1.2 \leq |\eta| \leq 2.2$ pseudorapidity, as well as measure muon tracks over the entire azimuth.

2.3 PHENIX Muon Arms

The muon arms have the ability to measure muons at forward and backward rapidities. Those muons are extremely important for the detection of Drell-Yan processes as well as for the production of vector mesons and heavy quarks. The Drell-Yan process occurs when a quark of one hadron and an antiquark of another hadron annihilate.

The muon arms have great importance in the spin physics program at RHIC, since they are used to reconstruct single muons with high transverse momentum (p_T). Those single muons are an essential tool for studies of the production of W bosons.

The data used for the analysis in this thesis primarily consist of data collected from the muon arms.

Each muon arm includes two different sub-detectors: the Muon Tracker and the Muon Identifier. The Muon Tracker is responsible for momentum measurements, while the Muon Identifier is responsible for the separation of muons from hadrons. The Muon Tracker in the north muon arm is 1.5 meter longer than the Muon Tracker in south muon arm (permitting removal of the PHENIX magnet from the collision hall).

2.3.1 Muon Tracker Sub-detector

The Muon Tracker sub-detector (MuTR) has a spatial resolution of approximately $100\text{ }\mu\text{m}$, which is around $\sigma(M)/M = 6\%/\sqrt{M}$ to the relative mass resolution, which permits separation of ρ/ω peak from ϕ , J/ψ and ψ' , and satisfactory separation of Υ and Υ' .

As seen in Figure 2.4, MuTR is equipped with three stations of cathode-strip tracking

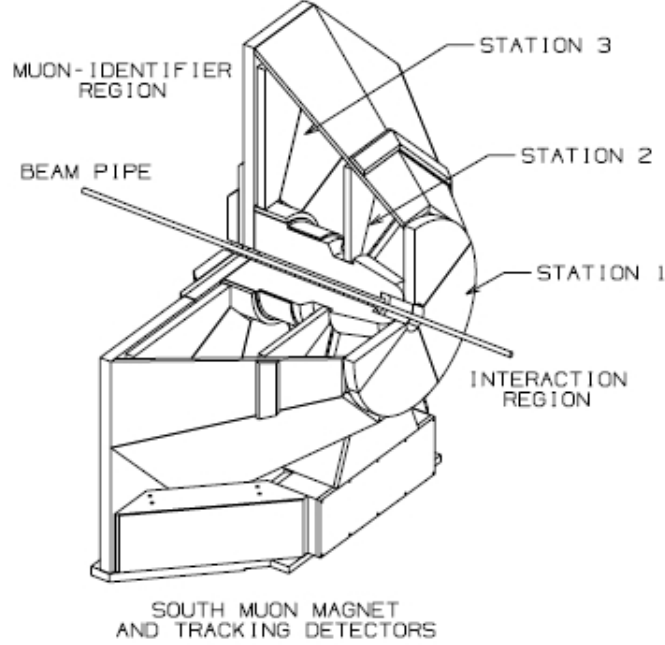


Figure 2.4: Drawing of the south Muon Tracker sub-detector [6].

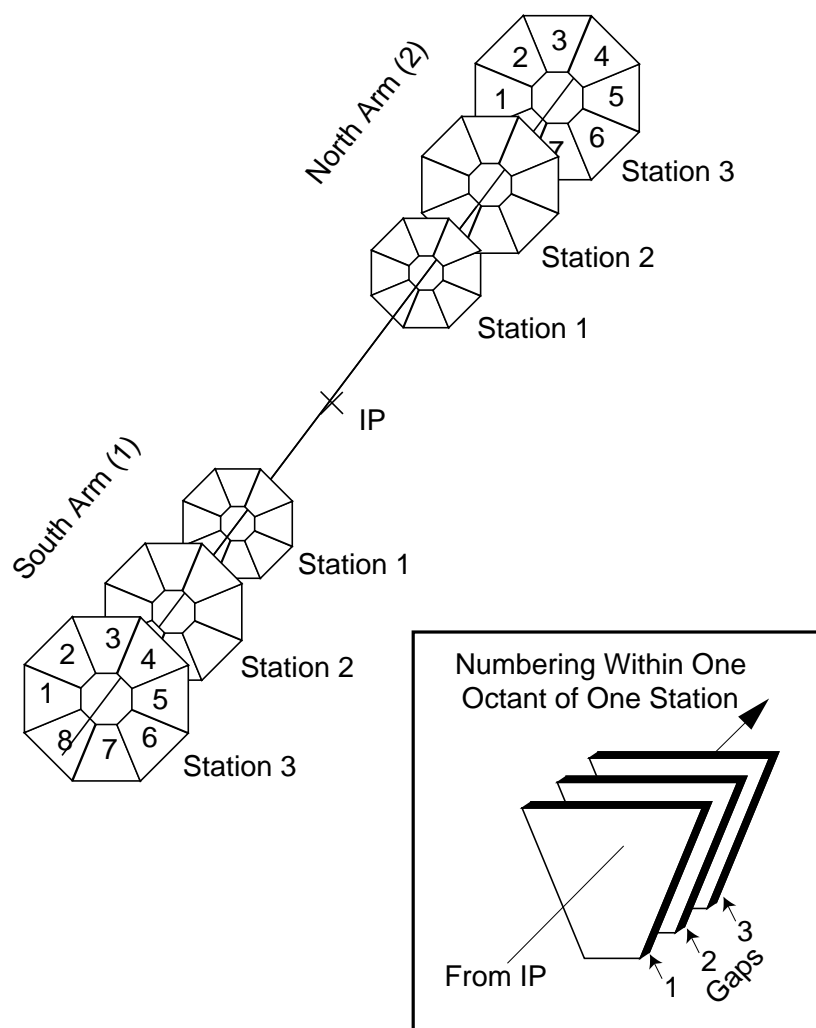
chambers. A more detailed view of those three stations is shown at Figure 2.5. There are three gaps in the first and second stations and two gaps in third station. In every gap there is a combination of two 1 mm wide cathode strips with an almost azimuthally running anode wire plane in between. In the first plane, cathode strips are perpendicular to the anode wires, while in the second plane they make a $\pm 11.5^\circ$ angle from the perpendicular strip. This configuration of cathode strips results in a resolution of $100 \mu\text{m}$. The operational voltage of the anode wires is 1850 V.

The momentum of the track of the charged particle in the magnetic field is calculated by:

$$p = q \cdot B \cdot R \quad (2.2)$$

where B is the magnetic field strength, q is the charge of the particle and R is radius of the sphere on which lies the trajectory which the particle makes while moving in the magnetic field. The magnets in the north and south arms are different in

Muon Tracking Nomenclature



W. Kinnison, 9/13/97

Figure 2.5: The MuTR stations and their numbering scheme [6].

size, but both provide $\int B \cdot dl \sim \text{T}\cdot\text{m}$ at a 15° polar angle. More details about the PHENIX magnets can be found in [32].

2.3.2 Muon Identifier Sub-detector

Another detector which is a part of both muon arms is the Muon Identifier sub-detector (MuID). The MuID is responsible for separating muons from hadrons. The amount of hadron background reduced by the MuID is huge thanks to the size, segmentation, and placement of the absorber material which is implemented in the muon spectrometers. Because of ionization energy loss [30], muons going through absorber lose a constant amount of energy. Hadrons also interact with absorber material. Those interactions make hadrons lose all or a significant amount of their energy. Thus, the hadron flux inside the absorber decreases due to penetration depth.

After the initial collision produced particles first reach the “nosecone” absorber material which is located immediately before the first station of the MuTR. This material is approximately 80 cm thick and represents about $5 \lambda_I$ of integrated nuclear interaction length. The muon magnet backplate is the next absorber material. It is 20 cm thick in the south muon arm. The muon magnet backplate in the north muon arm is 30 cm thick, due to different sizes between north and south muon arms. The muon magnet backplate is placed right after the MuTR and is followed by four layers (10, 10, 20, and 20 cm thick) of muon identifier detector. The schematic picture of the absorber material in the south muon arm is illustrated in Figure 2.6.

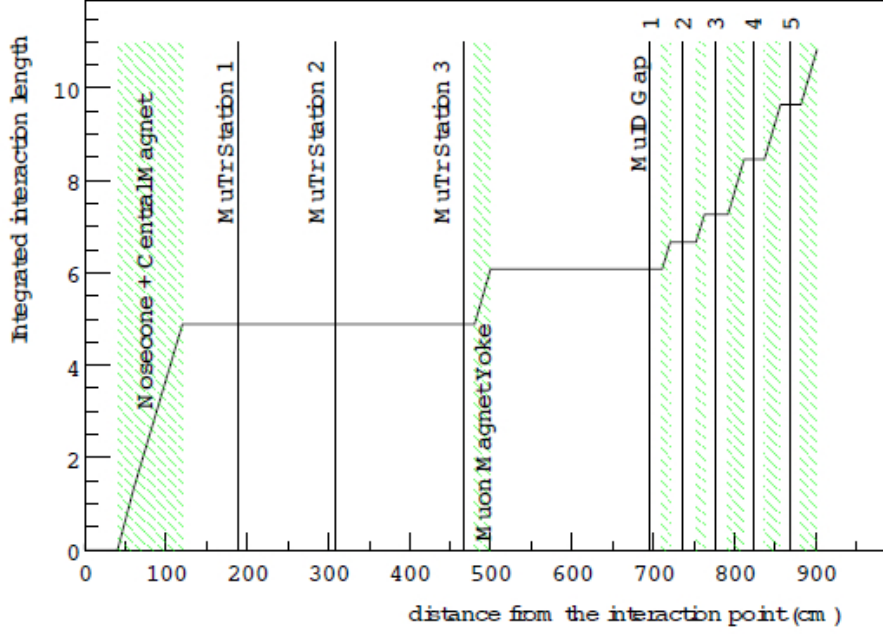


Figure 2.6: Schematic view of the absorber materials in the south muon arm [6].

The absorber material in the MuID provides space for five instrumented gaps (layers) in the MuID. Those gaps are number from 0 to 4, where the gap 0 is closest to the collision point and the gap 4 is farthest. The MuID detector contains steamer tubes, “Iarocci Tubes”, which are 8.35 cm wide, 1.3 cm thick and some are over 2 m long. Each of these tubes is divided into eight 9×9 mm cells, each equipped with $100 \mu\text{m}$ anode wires located inside the graphite-coated plastic cathode box, as illustrated in Figure 2.7. In order to increase efficiency for the detection of the particles, the tubes are ganged into two rows, called “two-packs”, displaced by half a cell. The tubes are operated at 4500 V.

There are six panels around the square beampipe hole in every MuID gap (Figure 2.8). Each panel has horizontally and vertically oriented layers. In total, there are 6140 “two-packs” in the MuID. Each “two-pack” registers signal from particles which deposit sufficient energy.

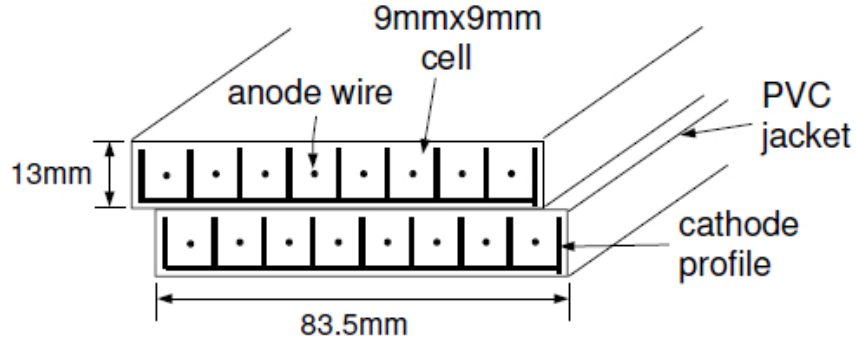


Figure 2.7: Cross section of a two-pack assembled from Iarocci tubes [6].

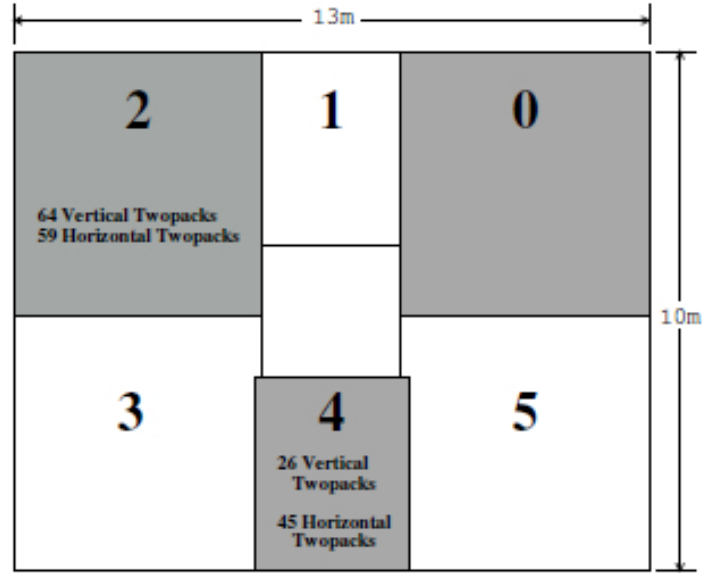


Figure 2.8: Schematic view of a MuID layer from the interaction point. The panels are numbered from 0 to 5 in the clockwise direction [6].

2.4 Reconstruction of Tracks in the Muon Arms

All online information recorded by the MuTR and MuID are combined in order to reproduce the tracks of particles in the muon arm. The reconstruction process is done offline and important information is recorded. The algorithm used for reconstruction begins by forming the “roads” in the MuID. Since in each gap we have horizontally and vertically directed “two-packs”, the maximum possible number of signals is two. For each orientation, one dimensional “roads” are created by fitting the signals with a line. Afterwards, those “roads” are merged, creating two dimensional “roads”. A detailed description of the MuID “road” creating process is provided in [33].

After the merging process, each possible two-dimensional “road” is matched with tracks reconstructed in the MuTR. Particles passing through the MuTR stations are later combined to create “clusters”. Later, the “clusters” located close to each other are combined by a linear fit to create the MuTR “stubs”. Each of those “stubs” provides information in the corresponding station in two dimensions because strips in the layers have two directions.

After all “stubs” are created, a tracking algorithm matches tracks with a “roads”, by picking up the closest “stubs” from the MuTR station 3 for every “road”. Once the initial matching is done, the tracking algorithm extrapolates to the stubs in stations 2 and then 1 in order to create an entire track. Once the track is entirely reconstructed, one obtains information about the momentum of particle and other relevant information.

2.5 Minimum Bias Trigger

The BBCLL1 trigger is so called minimum bias (MinBias) trigger used to select Cu+Cu collision events. The “MinBias” trigger selects least biased events, for example for the most central collisions, the efficiency for triggering the event is almost 100%, while it drops for the peripheral collisions. For an event to be selected by the “MiniBias” trigger, the event must at least have one registered signal in each of the four Beam-Beam Counters, and should have a collision vertex within ± 37.5 cm of the PHENIX origin.

2.6 PHENIX Dataflow

The PHENIX Data Acquisition system (DAQ) is responsible for collection of raw data. This information is written to PHENIX Raw Data Files (PRDF). The size of those files is typically 2 GB. Later, each PRDF is converted into a Data Summary Tape (DST) files and subsequently into picoDST files. A DST contains information about signals in each detector, while a picoDST contains track-by-track information (in the muon arms for instance). Collected picoDST files later are converted into femtoDST files, which are then ready for final analysis.

Chapter 3

Single Muon Analysis

3.1 Overview

In this chapter, the measurement of the single muons produced from semileptonic decays of heavy flavor mesons created in Cu+Cu collisions at $\sqrt{s_{NN}} = 200$ GeV is presented. In our analysis, we define collisions by three different intervals of centrality: most central collisions (0% - 20%), mid-central collisions (20% - 40%) and peripheral collisions (40% - 94%). Measurement of the single muon yield is done for $1.4 < \eta < 1.9$ rapidity and $1.0 \text{ GeV}/c < p_T < 4.0 \text{ GeV}/c$ momenta range, for all centralities. The data used for our analysis was collected during PHENIX Experiment RHIC Run-5 in 2005.

Later in this thesis, those measurements will be compared with the measured single muon yield in p+p collisions at $\sqrt{s_{NN}} = 200$ GeV, in order to calculate the nuclear modification factor.

As described in Chapter 2, the MuID detector contains multiple layers. In the last layer (Gap 4), all reconstructed tracks are considered to be heavy flavour muon candi-

dates. However, many of those tracks do not come from heavy flavor mesons. Those tracks are constitute a background. Unfortunately, it is impossible to distinguish such tracks in the PHENIX muon arms on an event-by-event basis. So, we subtract this non-heavy flavor background in a statistical manner.

Statistical subtraction of the background results in the single muon yield. Estimation of the background in Gap 4 is done by using a data driven Monte Carlo simulation of light hadron decay, called a “Hadron Cocktail”. Figure 3.1 shows the results of the subtraction procedure, to obtain the heavy flavour muon signal. (Triangles are single muon yields, stars are backgrounds, and circles are inclusive spectra).

As indicated in Figure 3.1, there is a large amount of background, dominantly coming from light hadrons decaying between the absorber and collisions vertex. The background consists of two main components: *Decay Muons* (DM) produced from the decay of light hadrons, and *Punchthrough Hadrons* (PH) which are hadrons produced at the collision vertex and reach the last MuID gap.

Decay Muons are the largest background component, especially at low momenta. The dominant source of those are the kaons and pions. Those particles are either produced directly or via decays. The inclusive branching ratio for charged kaons into muons is 99.98%, and for charged pions into muons is 66%.

The distance travelled by kaons and pions before decay is on average two orders of magnitude smaller than the distance between the collision point and the absorber. This means that relatively few kaons and pions reach the absorber before they decay.

The decay probability of kaons and pions into muons can be expressed:

$$P(\Delta z) = 1 - e^{-\frac{\Delta z}{\gamma c \tau}}. \quad (3.1)$$

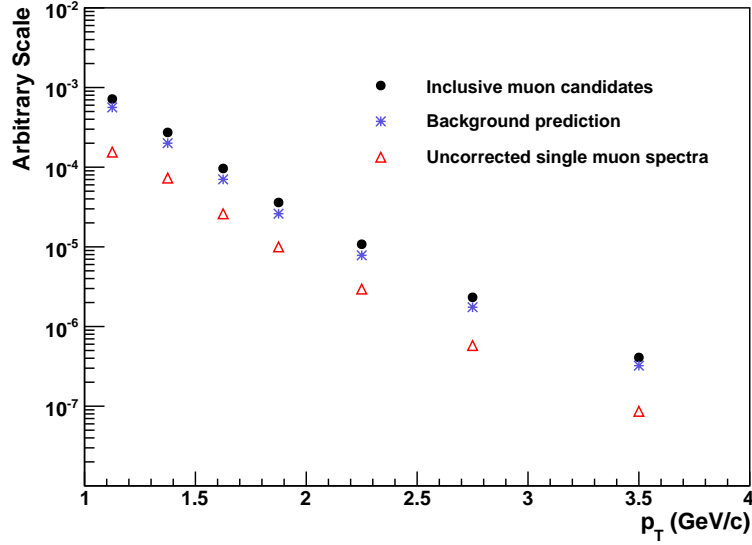


Figure 3.1: Representative muon inclusive spectrum (solid circles), prediction for total background (asterisks), and uncorrected single muon yield (triangles) which have been reconstructed in the south arm [6].

The probability of light hadron decay into muons is larger away from the absorber than close to the absorber. So, the vertex distribution of decay muons increases linearly with distance. Since DM are the largest contribution to the total inclusive spectra, the total sample of muon candidates also increases linearly with increasing distance from absorber (Figure 3.2).

The background contribution of punch-through hadrons is larger at high momenta. Light hadrons produced within the acceptance of the muon arms reach the absorber. Since those hadrons can interact with the material, the hadronic flux decreases with the number of interaction lengths of the absorber. Since the length of absorber between the collision point and MuID is quite large, very few light hadrons penetrate the entire detector and are detected at MuID Gap 4. Also, punch-through hadrons exhibit very small vertex dependence. Ultimately, the total number of punch-through hadrons are comparable to the number of muons resulting from the decay of heavy flavor.

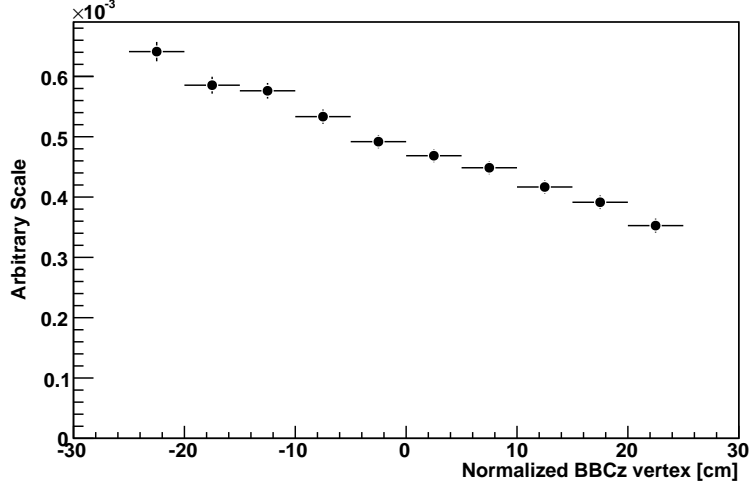


Figure 3.2: The Vertex position along the z-axis for the muon candidate tracks in the north arm, normalized with the event vertex z-coordinate distribution, BBCz [6].

Light hadrons stopped at MuID Gap 2 or Gap 3 are not considered single muon candidates, however, those tracks are very helpful in order to properly identify the background in MuID Gap 4. Those hadrons primarily stopped in the material due to nuclear interactions. Figure 3.3 shows that the of the muons produced from the decay of hadrons are within the peak, and hadrons which did not decay into muons are reconstructed in the tail. This is due to ionization energy loss, $-dE/dx$. Muons passing through material lose energy. A clean sample of hadrons can be obtained by choosing tracks which are beyond the peak. Those hadrons are called “stopped hadrons”.

3.2 “Hadron Cocktail”

Unfortunately, the PHENIX muon arms can not characterize the punch-through hadron yield at Gap 4; we need a Monte Carlo simulation in order to properly estimate the hadron background. Since there are no measurements of light hadrons at forward rapidity acceptance, the background is not well constrained. For that rea-

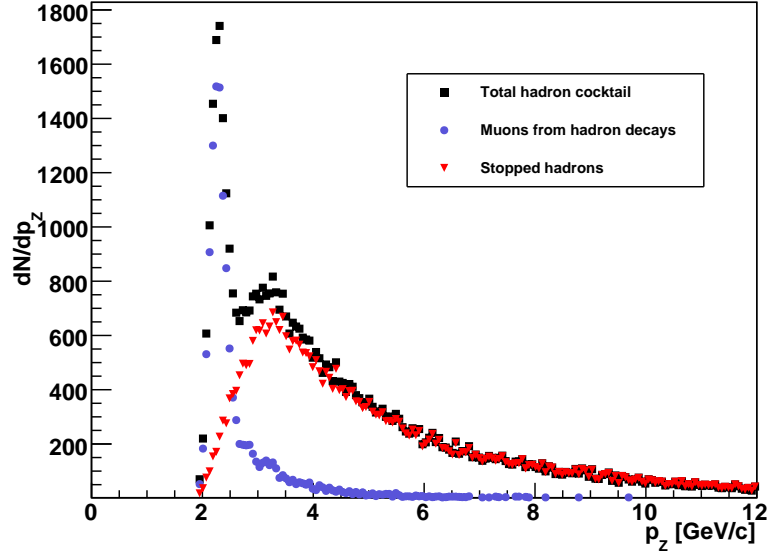


Figure 3.3: The distribution of the longitudinal momentum for tracks stopping in Gap 3 which is produced in the light hadron simulation [6].

son, we introduced a “Hadron Cocktail” in our analysis: a full-scale data-constrained Monte Carlo simulation including the full PHENIX detector geometry using the GEANT-3 package [34]. The hadron cocktail generates a prescribed mix of kaons and pions with specified p_T spectra within the acceptance of the muon arms as input. Later, those generated particles are propagated and subsequently reconstructed using the muon arm tracking software. This propagation is done using GEANT software simulation of the full geometry and material of the PHENIX detector. After reconstruction, the tracks are embedded into real Cu+Cu events. This reproduces the high multiplicity environment detector occupancy present during heavy ion collisions. Once the tracks are embedded, we normalize the input of hadron cocktail and adjust the p_T shape in order to match the prediction of stopped hadron yields in Gap 3 with the measured stopped hadron yields from data. We make sure that the simulation agrees with the measured hadron yield in Gap 2. Also, the shape of the measured vertex distribution is reproduced via the hadron cocktail input.

3.3 Signal Production

In our analysis we measure the invariant single muon yield separately for each muon arm. First, we observe the raw yield of single muons and subsequently convert it to an invariant yield. Once the single muon yield is converted, it is corrected for the finite acceptance of the detector and the efficiency of the selection criteria.

$$N_\mu(p_T) = \frac{1}{2\pi p_T} \frac{1}{dy dp_T} \frac{N_{I,raw} - N_{C,raw}}{N_{MB} \cdot A\epsilon_\mu} \quad (3.2)$$

Equation 3.2. provides the calculated invariant single muon yield $N_\mu(p_T)$, where $A\epsilon_\mu$ is the acceptance and efficiency correction factor, N_{MB} is number of events analysed in terms of minimum bias, $N_{I,raw}$ is the yield of inclusive tracks, and $N_{C,raw}$ is the yield of background. The extraction process of single muon signal is done by the following consecutive steps:

- The extraction process starts with preselecting the sample data of events of Cu+Cu collisions by the MinBias trigger.
- For N_{MB} , we need so-called “good” MinBias events. So after preselection, we perform initial QA (quality assurance) in order to define the “good” N_{MB} .
- As mentioned above, the invariant single muon yields are measured separately for North and South arms. Therefore the spectra for negatively charged particles are reconstructed in both arms separately.
- Since we want to select only stopped hadrons, in Gap 2 and Gap 3 we make a cut on longitudinal momentum.
- The next step is a so-called “analysis cut”, which is a set of track selection criteria. The kept track yields in each gap of both arms are converted to raw

invariant yields, normalized by the total number of events N_{MB} and corrected by a phase-space correction process.

- After normalization and correction, we start simulations. For simulations, we use several hadron cocktail packages, each of those packages are equipped with FLUKA or GHEISHA shower code. In combination with shower code, we use the specified modified value of nuclear interaction cross section for the absorber material. All of this is done using the GEANT Monte Carlo framework. All those cocktail simulations differ only by choice of the shower code and nuclear interaction cross section.
- The analysis cuts for data are identical to the cuts for simulations in Gap 2, Gap 3 and Gap 4, in order to be able to make comparison between cocktail packages and the data. The hadron flux produced by simulations of stopped hadrons is normalized for approximate matching of the data in Gap 3.
- After the matching process, the input transverse momentum spectra of light hadrons is modified multiple times until the simulation output matches the data for the full transverse momentum in Gap 3.
- For each muon arm, multiple tuning of the input spectra is performed separately, for each cocktail simulation. As an outcome, we end up with two different input spectra and both of them are averaged for both arms, in order to create one input spectrum for each cocktail package.
- The simulation should reproduce the vertex dependence of the decay muon inclusive yield very precisely. Also, simulation should match the stopped hadron data in the shallow gaps. Coincidence of the output from each simulation with data is checked at the same time in Gaps 2, 3 and 4.
- For each transverse momentum bin, predictions are taken in account only if they satisfy matching criteria. The cocktail simulations for the yield in Gap 4

are averaged to obtain the value $N_C(p_T)$ which is the predicted background for the corresponding transverse momentum bin.

- The muon yield is computed and corrected for the detectors acceptance and efficiency.
- Finally, the muon yield, computed and corrected for each muon arm, is combined in order to get the muon yield resulting from heavy flavor decay.

3.4 Acceptance and Efficiency Corrections

PHENIX has a full detector response implemented in the GEANT 3 package. The efficiencies for the muon spectrometer were very stable over the course of the multiple month period in which data were recorded. Realistic efficiencies are implemented in the simulation framework on a run basis over the course of data runs included in the full dataset.

Areas of differing acceptance between data and simulation are removed from both datasets using reliable geometric acceptance cuts. The extent of the remaining discrepancy serves as a direct source of systematic uncertainty in the final measurements of the p+p transverse momentum spectra and nuclear modification factor. An uncertainty in the acceptance \times efficiency of $\sim 8\%$ is assigned based on hit map comparisons in the MuTR and MuID detector layers.

Due to the performed analysis cuts and geometric acceptance of the muon arms, the sample of reconstructed single muon tracks must be corrected to obtain the yield of heavy flavor muons entering the muon arms. The efficiency for reconstructing tracks depends on the performance of the detector. This means that at the last step of the analysis, one has to make corrections to the uncorrected single muon yield, and those corrections must be done with taking in account acceptance \times efficiency factors ($A\epsilon_\mu$).

For the calculation of $A\epsilon_\mu$, simulations starting exclusively from muon tracks have been performed. The simulation starts with the generation of single muon tracks within the transverse momentum interval 0.8 GeV/c - 10.0 GeV/c and rapidity interval $1.1 \leq |y| \leq 2.1$. In order to have sufficient statistics at high p_T , several simulations have been performed separately, where the muons are thrown with identical shape with the initial p_T close to the low end of the analyzed bin. A more detailed description of this process can be found here [15].

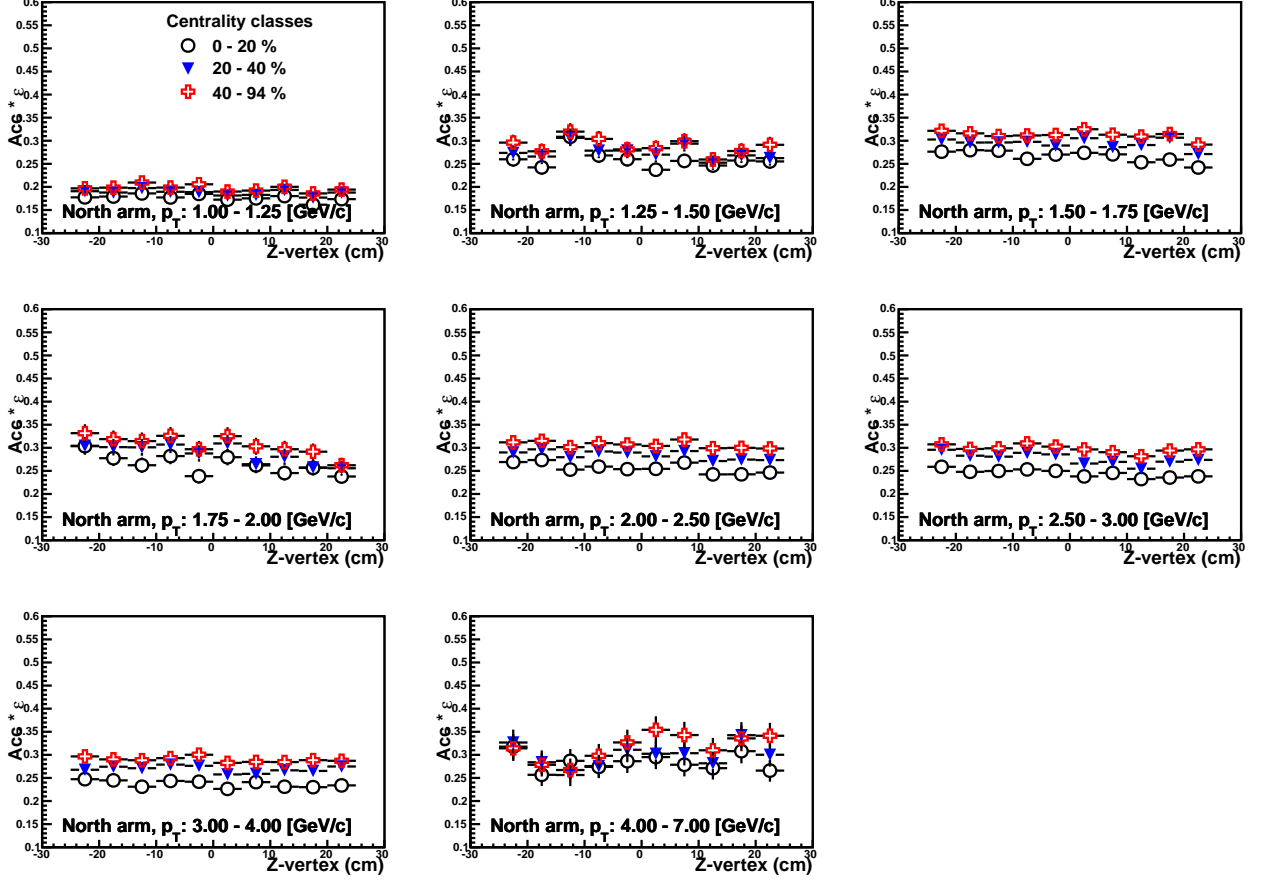


Figure 3.4: Dependence of A_{ϵ_μ} correction on z-vertex position and p_T bins for every centrality class (North arm) [6].

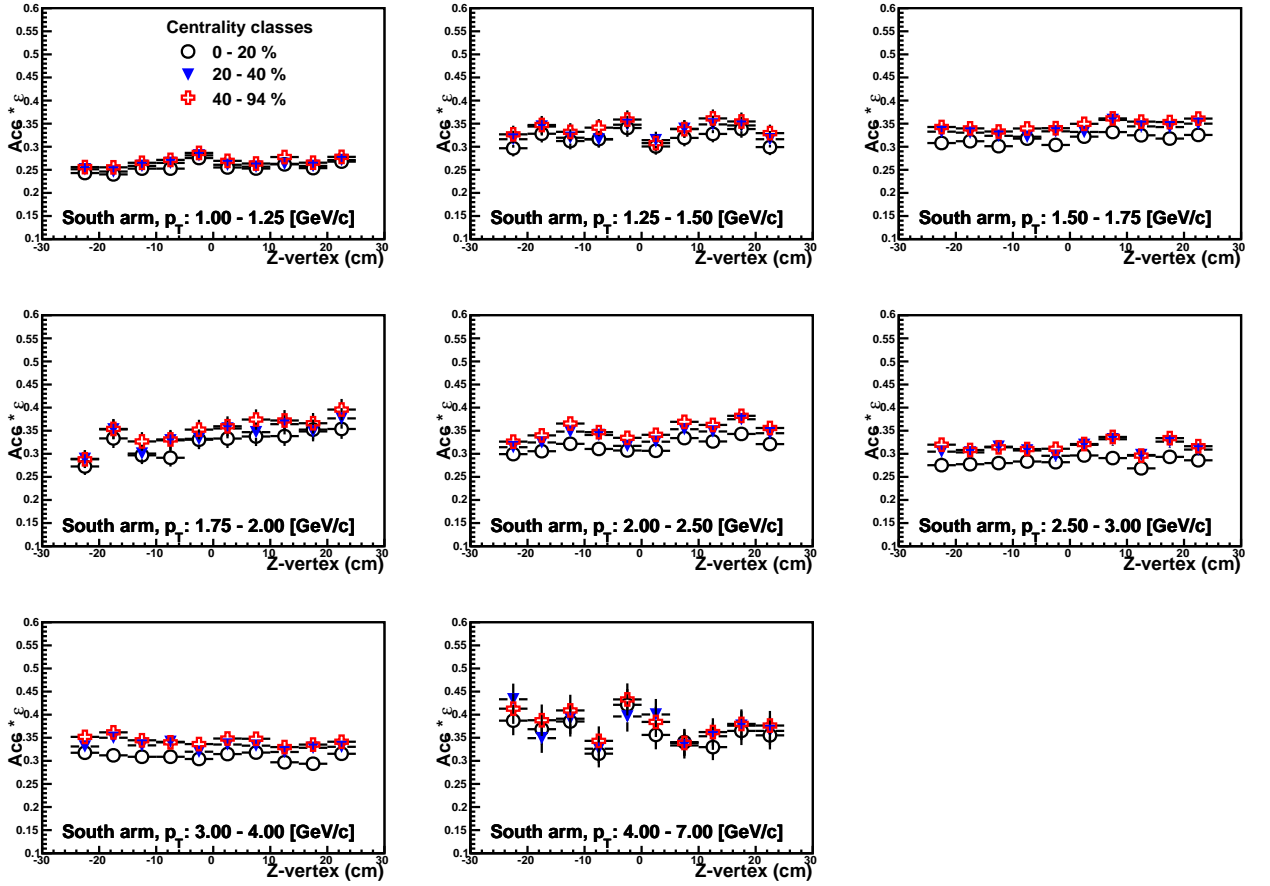


Figure 3.5: Dependence of $A\epsilon_\mu$ correction on z-vertex position and p_T bins for every centrality class (South arm) [6].

The Acceptance \times Efficiency factor depends on the kinematics of the reconstructed muon track. Thus $A\epsilon_\mu$ should be calculated separately for each centrality class, each p_T bin, and each z-vertex position as:

$$A\epsilon_\mu(\Delta p_T, \Delta z) = \frac{N_{reco}(\Delta p_T, \Delta z)}{N_{thrown}(\Delta p_T, \Delta z)} \quad (3.3)$$

where $N_{thrown}(p_T, \Delta z)$ is the total number of the single muon tracks thrown within the given Δp_T bin and Δz z-vertex position, and $N_{reco}(\Delta p_T, \Delta z)$ is the total number of simulated muon tracks reconstructed after applying the analysis cuts.

Figures 3.4 and 3.5 illustrate the dependence of the simulated Acceptance \times Efficiency corrections for each muon arm on the z-vertex position, centrality class, and p_T bin. Since the dependence of $A\epsilon_\mu$ on the z-vertex position is fairly small, we can apply the $A\epsilon_\mu$ factors depending only on transverse momentum bin and centrality classes. In Figure 3.6, we clearly see the difference for each centrality class.

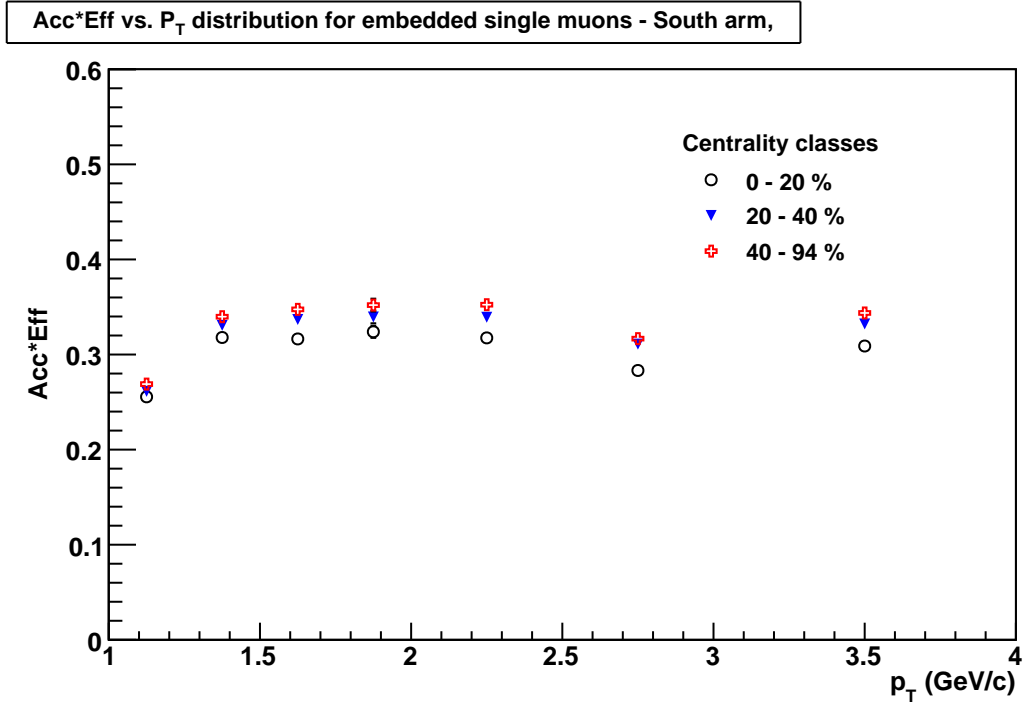
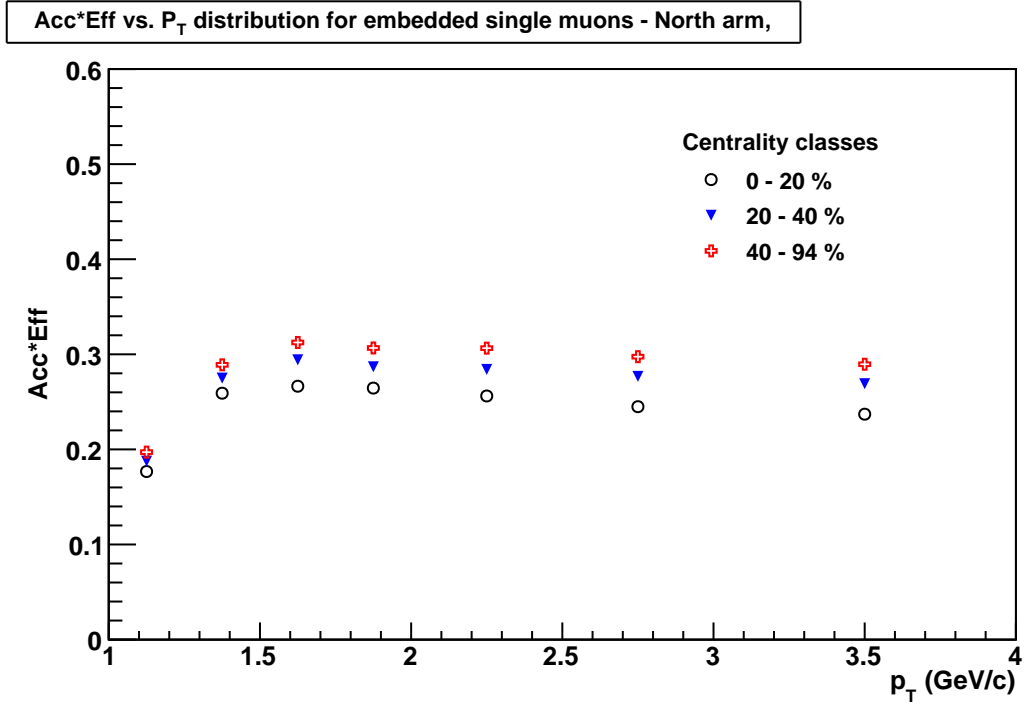


Figure 3.6: Acceptance \times Efficiency correction factors depending only on p_T for all centrality classes: north arm (upper) and south arm (lower) [6].

Chapter 4

Background Monte Carlo Simulation

4.1 Overview of “Hadron Cocktail”

The “Hadron cocktail” is a Monte Carlo simulation of the light hadron background produced in the muon arms. It was implemented in order to determine the amount of background which plays a significant role in our analysis.

The transverse momentum distribution of $\pi^\pm, K^\pm, p, \bar{p}, K_L^0, K_S^0$ particles are generated as input using the GEANT simulation package. Since there are almost no measurements of light hadrons spectra at p+p and Cu+Cu collisions for the $1.4 < |y| < 1.9$ rapidity interval, we decided to select measurements of the π^0 spectrum at $y \sim 0$ in p+p collisions as an initial estimate. Also, one must convert the measured spectrum into particle yields since it was measured as an invariant cross section.

After construction of the π meson distributions, we determine the input for kaons

by using the measured K/π ratio. This ratio depends on transverse momentum and is formed by combining STAR and PHENIX measurements of pions and kaons [35].

The light hadrons are propagated using the GEANT 3 simulation package [34], which includes the exact geometry of the PHENIX detector. The number of simulated tracks in MuID gaps 2, 3 and 4 depends on the hadron track propagation and absorber. In GEANT, shower code models the strong interaction physics for the hadron tracks passing through the absorber.

Two different hadronic interaction packages within the GEANT framework are used for our analysis: GHEISHA and FLUKA. Unfortunately, those two packages are not able to reproduce the measured hadronic flux in all MuID gaps. A particle weighting scheme has been introduced which permits the input hadron distributions to the hadron cocktail to float. A set of hadron cocktail simulations are generated with a modified value of the experimentally observed hadron interaction cross section in order to provide the best matching of hadron cocktail simulation distributions to PHENIX data.

In Cu+Cu and p+p collisions, the spectra of the background track yields are subtracted from the yield of inclusive muon candidates in order to extract the heavy flavor yields. Since GEANT 3 does not have ability to accurately propagate showering hadrons through the 1.5 m of absorber the hadron cocktail calculations are not able to reproduce the observed data yields in Gaps 2, 3 and 4 of the MuID detector. Because of that, we introduce a set of hadron cocktail packages with modified hadron interaction cross sections in order to produce the background estimations. The set of background estimates are combined in a weighted fashion in order to determine the central values. The systematic uncertainty produced by this package mismatch is assigned and used together with other sources of systematic uncertainty for the determining the central values for the p+p cross section and R_{AA} .

Each hadronic shower code has been modified in order to allow the hadronic interaction of pions and kaons in steel to be scaled for FLUKA and GHEISHA, respectively. FLUKA hadron simulations produce less particles than GHEISHA. Therefore, the cross section in FLUKA is increased (and decreased in GHEISHA). There are three different packages of FLUKA (FL105, FL106 and FL107) and two different packages of GHEISHA (GH92 and GH93). The names of each package represent the percentage scaling for the nuclear interaction cross section. In addition, each package represents a total of 10^{10} simulated hadrons.

4.2 Initial Data Production

For the nuclear modification factor calculations in our analysis, we used datasets of Cu+Cu and p+p collisions at the center of mass energy per nucleon nucleon collisions $\sqrt{s_{NN}} = 200$ GeV.

For the p+p data recording, three kind of triggers have been used. The first trigger is the MinBias trigger, which requires at least one hit registered in each Beam Beam Counter subdetector. Around 55% of the total p+p inelastic collision cross section is covered by MinBias trigger. The RHIC Run-5 integrated luminosity sampled with the MinBias trigger is around 44.3 nb^{-1} .

The other two triggers are the muon enriched triggers which use information collected in the MuID detector. The difference between those two triggers is the different requirements for the penetration depth for muon candidates inside the MuID detector. One trigger requires that at least one muon candidate should reach Gap 4 in MuID. This trigger is called the Deep Trigger. The other one requires that at least one muon candidate should reach Gap 2 in MuID and is called the Shallow Trigger.

The Cu+Cu collision data used for our analysis were selected solely by the MinBias

trigger. The coverage of the MinBias trigger for Cu+Cu collisions is different from p+p collisions. It is approximately 94% of the total inelastic cross section.

Centrality Selection

As mentioned in Chapter 1, the centrality of the collision can not be measured directly at RHIC. However, we can perform experimental measurements of particle multiplicity and combine it with the Glauber model based Monte Carlo simulation, in order to estimate impact parameter b , number of participant nucleons per heavy ion collision N_{part} , and the number of the subsequent inelastic binary nucleon-nucleon collisions N_{coll} .

For the estimation of those variables and also for determination of the z-coordinate of the collision vertex in p+p and Cu+Cu collisions, the Beam Beam Counters (BBCs) are used. For example, centrality in Cu+Cu collisions is determined by energy deposition in the BBCs.

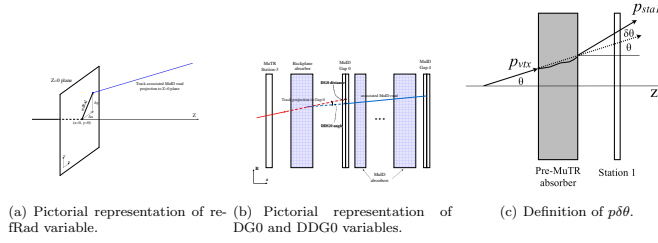
In our analysis we use three classes of centrality: 0 - 20 % (central), 20 - 40 % (mid-central), and 40 - 94 % (peripheral). For qualitative estimation of the centrality classes, heavy ion collisions at PHENIX are required to be within 30 cm of the center of PHENIX detector along the beam axis.

4.2.1 Variables in the Analysis

In our analysis, for the measurements and the simulations, we used sets of variables indicated in Figure 4.1:

Each of the quantities in Figure 4.1 was carefully simulated and compared to realistic backgrounds presented in data [6] [15] in order to obtain optimal cut values.

- **BBCz** - The event z-vertex position measured by the BBC detector.
- **refitZ** - The z-vertex position of a track provided by the muon track reconstruction framework, taking the momentum of this track reconstructed in Station 1 of the MuTR and projecting back to the collision vertex through the nosecone absorber.
- **Number of MuTR hits** - Any track passing through the three stations of the MuTR can register up to 16 hits per arm.
- **refR** - The refR variable, indicated in Figure (a), is the projected radial offset of the track associated MuID road at the $z=0$ plane. The refR variable is calculated from $\sqrt{\Delta x^2 + \Delta y^2}$, where Δx and Δy represent the separate offsets at $z=0$, which are obtained by extrapolating to the $z=0$ plane the one-dimensional slope in either x or y of the MuID road through the gap 0 hit position.



- **Road Slope** - MuID road slope in Gap 0, $\sqrt{\left(\frac{dx}{dz}\right)^2 + \left(\frac{dy}{dz}\right)^2}$, which is used to eliminate tracks that point to the square hole in the absorber steel and MuID gaps.
- **DG0** - The 2D-distance (in centimeters) at Gap 0 between the MuID road projection and the MuTR track projection from Station 3 (Figure (b)).
- **DDG0** - The angle (in degrees) between the MuTR track projection vector from Station 3 and the MuID road projection vector (Figure (b)).
- **$p\delta\theta$** - The scattering angle of the track in the nosecone absorber, $\delta\theta$, scaled by the average of the momentum magnitude at the vertex and at Station 1, $\bar{p} = \frac{p_{vtx} + p_{sta1}}{2}$.
The $\delta\theta$ angle, indicated in Figure (c), can be calculated from the following:
$$\delta\theta = \cos^{-1} \left(\frac{\vec{p}_{vtx} \cdot \vec{p}_{sta1}}{|\vec{p}_{vtx}| |\vec{p}_{sta1}|} \right)$$
. The quantity \vec{p}_{sta1} is the momentum vector measured at Station 1, whereas, \vec{p}_{vtx} is the momentum vector at the event vertex estimated by the tracking algorithm. For a given track, the $\delta\theta$ angle essentially measures the extent of deflection due to multiple scattering and radiative energy loss occurring in the nosecone absorber. The angular deflection of a track in the absorber is expected to be inversely proportional to the momentum. Therefore scaling the scattering angle by the total momentum ensures, in principle, that the total distribution, $p\delta\theta$, remains approximately a Gaussian with constant width in all p_T bins.
- **δZ** - The difference between the event vertex reconstructed by the BBC and the vertex reconstructed from the muon reconstruction code, $\delta Z = BBCz - refitZ$. Those tracks which show large differences between the event z-vertex and the track fit vertex correlate strongly with those tracks exhibiting pathologically large $p\delta\theta$ values.

Figure 4.1: The description of the variables used for the measurements and the simulations [6].

4.2.2 Non-hadron Cocktail Background

The hadron cocktail is the primary basis for the estimation of the inclusive muon background. However, there is a small non-hadron cocktail background component, which is not reproduced by hadron cocktail. This non-hadron cocktail background is due to increasing background tracks for increasing transverse momentum. This background is estimated separately and is subtracted statistically from the inclusive muon yield.

This background is observed in the $p\delta\theta$ distributions that shows a broadened multiple peak in the higher transverse momentum bins. The broadening of the $p\delta\theta$ distributions is associated with poorly reconstructed tracks indicated by large δZ (Figure 4.2). The non-hadron cocktail background is then estimated and subtracted using $p\delta\theta$ and δZ . Once this background is subtracted, the $p\delta\theta$ distributions for the hadron cocktail reproduces the distribution observed in data.

Since the $p\delta\theta$ distribution is peaked at a constant value for all transverse momentum bins, tracks with $p\delta\theta$ value less than 0.2 are accepted. The non-hadron background is observed by inspecting the $p\delta\theta$ distribution inside and outside the δZ cut (Figure 4.2). The left panel of Figure 4.2 shows the $p\delta\theta$ distribution of the inclusive muon yield inside and outside the δZ cut. The right panel of Figure 4.2 repeats the fraction of the inclusive muon tracks outside the δZ cut and shows a scaled distribution of those inside the δZ cut.

The observed non-hadron cocktail background happens to be less than 1% of the total inclusive muon yield for the lowest transverse momentum bin, around 5% for the highest bin.

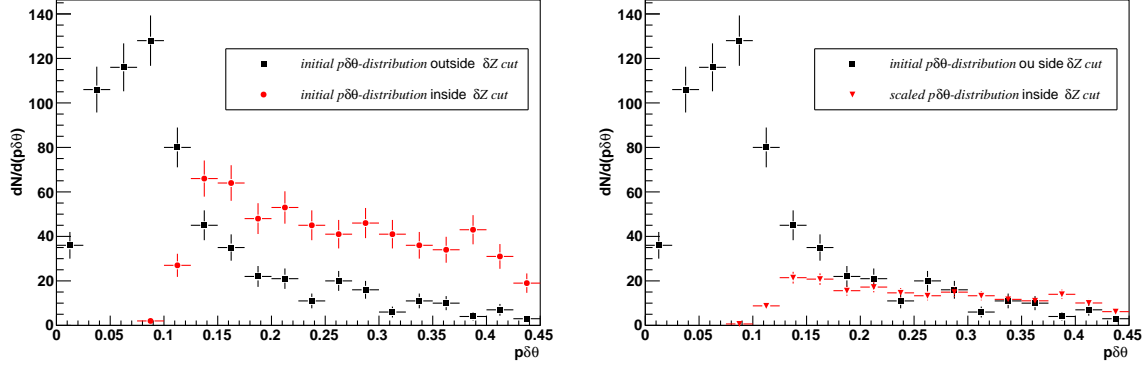


Figure 4.2: $p\delta\theta$ distributions of the stopped hadrons reconstructed in Gap 3 of the north arm for the transverse momentum range 2.5 to 3.0 GeV/c. The left panel shows the comparison between the raw distribution of $\delta Z < 2$ cm to the raw distribution for $\delta Z > 2$ cm. The right panel shows the comparison between the initial distribution of $\delta Z < 2$ cm with the initial distribution of $\delta Z > 2$ cm, which is scaled in order to match the tail of the $p\delta\theta$ distribution of $\delta Z < 2$ cm [6].

4.3 Matching of Data

The cocktail background simulation serves to predict backgrounds in Gaps 2 and 3 as well as 4. By iteratively “tuning” weights associated with the cocktail tracks and comparing to data for tracks stopping in Gap 2 and 3, it has been possible to adjust our cocktail to the observed background.

Measurements for all particles needed in the hadron cocktail are not available at RHIC for $y \sim 1.65$. Estimated transverse momentum distributions of π and K at $y \sim 1.65$ have been produced using analysis of all available data sets for $y=0$ and $y > 2.2$. Measurements for the remaining hadron distributions that contribute about 1% of the total yield are not available. In order to include these contributions in the hadron cocktail, transverse momentum distributions of kaons have been scaled by the ratio of the particle yields at $y=0$.

The range of the pseudorapidity in our analysis is $1.4 \leq \eta \leq 1.9$, while the acceptance of the muon spectrometer is $1.2 \leq \eta \leq 2.2$. The particles have been generated for

entire range of pseudorapidity.

In order to reproduce the high multiplicity environment in Cu+Cu collisions, the Cu+Cu hadron cocktail has been embedded in Cu+Cu minimum bias collisions. The track reconstruction algorithms are run on the combination of a single simulated hadron, which has been determined from the hadron cocktail input distribution together with additional hits associated with a sample event from a pool of minimum bias events. For the embedding process, the pool has sufficient size in order to minimize potential biases during the track reconstruction process.

The next step is applying the track based selection criteria. The data and each hadron cocktail package output are passed through the track reconstruction software. The particles are binned in transverse momentum p_T and normalized according to the z-vertex dN/dz . The hadron cocktail is initially generated with a flat dN/dz distribution and is normalized to provide the best overall data matching. There are two reasons causing a difference between the hadron cocktail p_T and dN/dz distributions and the corresponding data distributions:

- The failure of the simulation and hadron shower code to correctly reflect produced data which is compensated by producing a set of hadron cocktails with varying hadronic interaction cross sections.
- The difference between measured data and the particle input distribution of the hadron cocktail which is compensated by iteratively re-weighting the input particle's transverse momentum bins, in order to optimize the match between data and hadron cocktail for Gaps 2, 3 and 4 in MuID detector.

4.4 Systematic Uncertainty

The hadron cocktail which provides the essential background estimation, also creates some systematic uncertainties. The two main systematic uncertainties of the hadron cocktail are:

- σ_{SystPack} is the correlated systematic uncertainty associated with the implementation of the hadron cocktail simulation package. σ_{SystPack} is composed of two components: the uncertainty on the hadron cocktail input distributions and the MuID Gap3 and 4 efficiency matching as determined from the simulations. The uncertainty on the hadron cocktail input uncertainty is assigned a 20% uncertainty. The MuID Gap 3 to 4 efficiency match is assigned a 10% uncertainty. These two uncertainties are uncorrelated and added in quadrature are approximately 23%.
- The hadron package mismatch uncertainty $\sigma_{\text{PackMismatch}}$ characterizes, as a function of transverse momentum bin, the weighted dispersion of the different background estimations (i.e. hadron cocktail packages). A single hadron cocktail package represents a choice of a single hadron shower code and a particular hadronic cross section. The output of the hadron cocktail does not exactly match the data yields in MuID Gaps 2, 3 and 4. In order to determine the dispersion for a single hadron cocktail calculation, that cocktail is tuned four times so that it is made to separately match each of the MuID Gaps 2, 3 and 4. A fourth “optimal” tuning of each hadron cocktail represents a single best match to MuID Gaps 2, 3 and 4 simultaneously.

The dispersion in the Gap 4 yield of the four different tunings is used to calculate the value of $\sigma_{\text{PackMismatch}}$. The values for $\sigma_{\text{PackMismatch}}$ are calculated for both muon spectrometer arms and for each of the five hadron cocktail packages used in our

analysis. The mathematical details of the calculation are described in detail in Appendix A. Since the optimization is arm dependent, this uncertainty in the North and South arms is uncorrelated. The approximate magnitude of this uncertainty is 10 to 20% and varies with transverse momentum.

Another source of backgrounds are, the so-called non-hadronic backgrounds:

- Light hadron decay in the tracking volume between the front absorber and the final plane of the MuID.
- Muons from heavy flavor resonance with leptonic decay.
- Muons from Drell-Yan processes.
- Muons from light vector meson decay.

The background tracks from quarkonia, light vector meson decay and Drell-Yan processes have less contribution to the inclusive yields compared to background tracks coming from light hadron decays. The outcome from Monte Carlo simulations [36] is that the overall contribution to the final heavy flavor single muon transverse momentum yield is less than 5% over the entire transverse momentum range included into the analysis. The background tracks from Drell-Yan and light vector mesons is fairly small compared to the total number of background tracks in Gap 4. Neglecting those contributions, we summarize that the source of remaining tracks are the hadrons which penetrate the entire muon arm.

For the estimation of the effects of all analysis and cuts on the detector acceptance and efficiency for the reconstructing heavy flavor muon tracks, we used Monte Carlo simulation of single muon tracks into the muon arms kinematic acceptance. For the Cu+Cu collisions, the single muon tracks are embedded into the “MinBias” Cu+Cu data to account the effects of increased detector occupancy in Cu+Cu collisions. The

software trigger emulator was run for the hadron cocktail and single muon simulations in order to include effects from different muon triggers for the p+p data collection.

Table 4.1 shows the summarized final results for the uncertainties in the acceptance \times efficiency corrections and also other individual components which are included in quadrature to estimate the total σ_{A_ϵ} .

Table 4.1: Uncertainties in the acceptance and efficiency corrections. The individual components are added in quadrature to assign the total value of σ_{A_ϵ} .

	Component	Value
σ_{MuTr}	MuTr station data/MC	8%
σ_{MuID}	MuID Gap4 efficiency uncertainty	4.5%
$\sigma_{\text{run to run}}$	Run to run variation	2%
$\sigma_{\text{p-scale}}$	J/Ψ mass peak	1.5%
σ_{A_ϵ}	Total	9.5%

Table 4.2: Uncertainties in the single muon analysis. The individual components contribute to the final uncertainty as discussed in Appendix A.

Component	Value
Package mismatch	varies, of order $\sim 10\%$
Single package uncertainty	varies, of order $\sim 10\%$
Dispersion between packages	varies, from 10 to 20%
Acceptance and efficiency	9.5%
Arm mismatch	$\sim 20\%$

In addition, Table 4.2 is the summary of the systematic uncertainties associated with the determination of the transverse momentum spectrum and nuclear modification factor which are used for calculation of the central values described in Appendix A.

4.5 Single Muon Yield

For both p+p and Cu+Cu collisions the double differential heavy flavor muon invariant yield is defined by:

$$\frac{d^2 N^\mu}{2\pi p_T dp_T d\eta} = \frac{dN_I - dN_C - dN_X}{A\epsilon_\mu} \quad (4.1)$$

where the left side of the equation is the double differential invariant yield of heavy flavor single muons, dN_I is the inclusive muon track sample, tracks which passed all selection criteria and reached the Gap 4 in MuID detector, dN_C is the invariant yield of hadron background, dN_X is the invariant yield of the non-hadron cocktail background and $A\epsilon_\mu$ is the product of acceptance and efficiency corrections.

For p+p collisions the double differential invariant cross section is defined by:

$$\frac{d^2 \sigma^\mu}{2\pi p_T dp_T d\eta} = \frac{dN_I - dN_C - dN_X}{A\epsilon_\mu} \cdot \frac{\sigma_{BBC}^{pp}}{\epsilon_{BBC}^{c\bar{c} \rightarrow \mu}} \quad (4.2)$$

where σ_{BBC}^{pp} is the cross section measured in p+p collisions by Beam Beam Counter detectors and $\epsilon_{BBC}^{c\bar{c} \rightarrow \mu}$ is the BBC trigger efficiency.

A set of hadron cocktail calculations weighted by their ability to reproduce measured data are used for the final background contribution calculations.

4.6 Nuclear Modification Factor Calculations

Simplistic application of Equation 1.3 does not allow for the cancellation of systematic uncertainties in the hadron backgrounds that can be obtained by incorporating

both p+p and Cu+Cu data in the calculation of that background. Instead, the nuclear modification factor R_{AA} is calculated separately for the two muon arms for hadron cocktail background calculations weighted according to their ability to reproduce the both data sets:

$$R_{AA}^i = \frac{1}{\langle N_{coll}^{Cu+Cu} \rangle} \cdot \left(\frac{dN_{Cu+Cu}}{dN_{p+p}} \right)^i \quad (4.3)$$

where the index i denotes a hadron cocktail background calculation for the same set of physics used for the p+p and Cu+Cu data. The method of the R_{AA} calculations is described in detail in Appendix A.

The idea to introduce the method of the nuclear modification factor calculations via Equation 4.3 has been implemented in order to reduce the overall systematic uncertainties associated with the final R_{AA} calculation.

Chapter 5

Experimental Results

The methodology described in Chapter 4 is used to measure the p_T spectra of heavy flavor single muons in p+p and Cu+Cu collisions. The single muon p_T spectra in p+p collisions is later used to calculate the charm production cross section. Also in this chapter, the measurements of the nuclear modification factor for Cu+Cu collisions will be presented.

5.1 Single Muon Spectra

The p_T distribution of the differential cross section of muons from heavy flavor decay has been measured in the both arms independently at $\langle y \rangle = \pm 1.65$ and averaged (Figure 5.1). The measurements for both arms are combined in order to reduce systematic uncertainties. Those measurements are compatible within systematic errors. Following the method for central point determination described in Appendix A, the sources of systematic uncertainty have been combined to provide the final uncertainties.

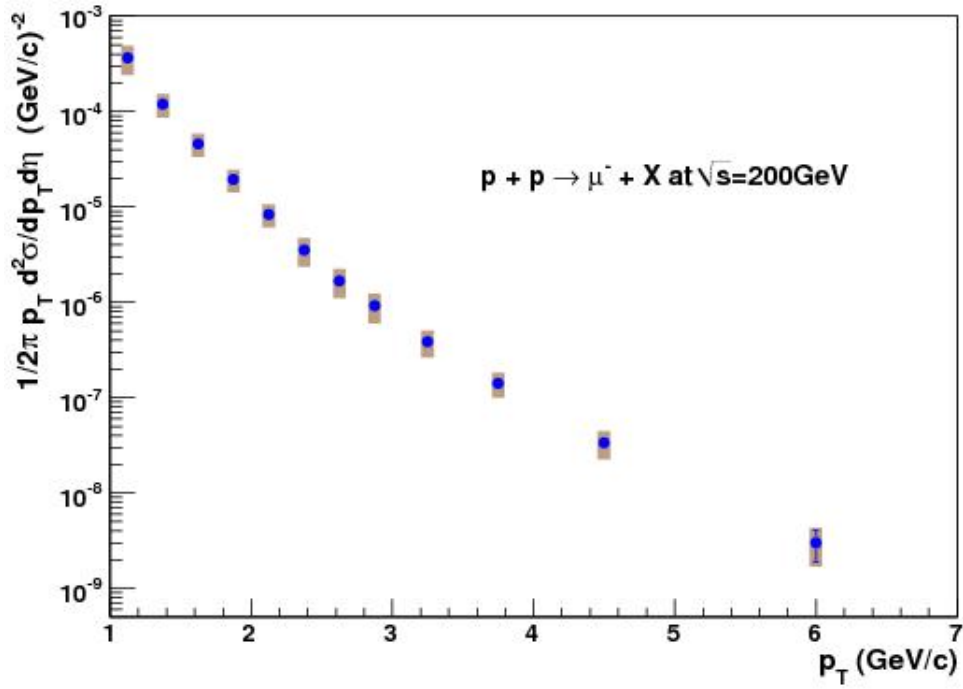


Figure 5.1: The p_T distribution of the differential cross section for the production of single muons from semileptonic heavy flavor decay in p+p collisions [37].

Figure 5.2 presents the p_T distributions of the invariant yields of negatively charged single muons from heavy flavor decay for all three centralities in Cu+Cu collisions and the p_T distribution of the invariant yield of negatively charged single muons from heavy flavor decay in p+p collisions.

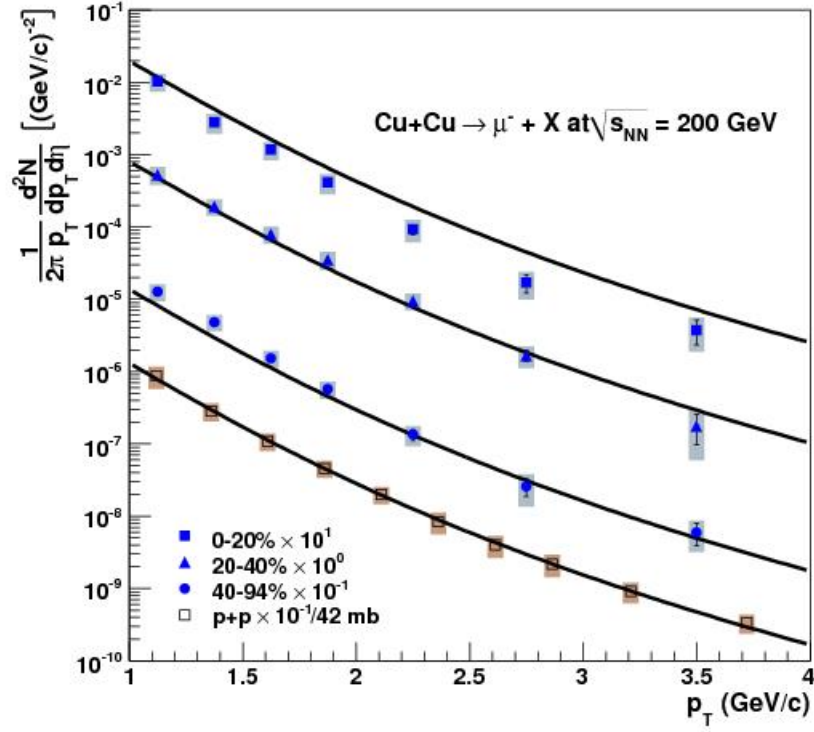


Figure 5.2: The p_T distribution of the invariant yields of single muons for all three centralities in Cu+Cu collisions, scaled by powers of ten. The p_T distribution of the invariant yield of single muons in p+p collisions [37].

5.2 Cross Section Measurements

In order to estimate the charm production cross section $d\sigma_{c\bar{c}}/dy$ at $\langle y \rangle = 1.65$, we use the p+p heavy flavor single muon transverse momentum spectrum. The range of transverse momentum for the single muon spectrum is from 1 GeV/c to 7 GeV/c. In order to estimate the full charm cross section one must perform a theoretical extrapolation for $p_T < 1$ GeV/c. The theoretical calculation we used is called Fixed-Order plus Next-to-Leading-Log (FONLL).

$$d\sigma_{c\bar{c}}/dy = \frac{1}{BR(c \rightarrow \mu)} \cdot \frac{1}{C_{e/D}} \cdot \frac{d\sigma_\mu}{dy} \quad (5.1)$$

Equation 5.1 is used to calculate the charm production cross section $d\sigma_{c\bar{c}}/dy$, where $BR(c \rightarrow \mu)$ is fixed at 0.103 in FONLL, the total muon branching ration of charm, $C_{e/D}$ is the kinematical correction factor for the different rapidity distribution of leptons and D mesons, and $\frac{d\sigma_\mu}{dy}$ is the integrated cross section of single muons over all p_T which is extrapolated from the smallest measured transverse momentum to zero GeV/c using FONLL. Because of the large amount of iron material between the interaction point and the muon spectrometer, the lowest measurement bin of transverse momentum is 1. GeV/c. Based on FONLL calculations, 6% of the total charm production cross section extends beyond p_T of 1 GeV/c. The integral of bottom quark decay is negligible compared to total integral spectrum, so its contribution is ignored. The statistical error of the integral of the measured heavy flavor muon transverse momentum spectrum greater than 1 GeV/c is calculated by summing the the statistical errors for each data bin.

The extrapolation method of the single muon transverse momentum spectra is given by Equation 5.2

$$d\sigma_{c\bar{c}}/dy |^{PHENIX} = d\sigma_{c\bar{c}}/dy |^{FONLL} \cdot Scale^{FONLL} \quad (5.2)$$

where $Scale^{FONLL}$ is defined by fitting the data spectrum to FONLL $E \frac{d^3\sigma}{dp^3}$. We use Equation 5.2 to calculate the charm cross section $d\sigma_{c\bar{c}}/dy$ at $\langle y \rangle = 1.65$.

The total systematic uncertainty of the charm production cross section is the combination of the data and theoretical uncertainties. In order to identify the data uncertainties, we fit the upper and lower data systematic uncertainties of the transverse momentum spectrum with the FONLL central value spectrum. This process gives the upper and lower bound $Scale^{FONLL}$ value. The extracted $Scale^{FONLL}$ uncertainty is about 35% of the data systematic uncertainties. The dominant theoretical uncertainties are associated with the scale and mass parameters. The transverse momentum spectrum is fit to the upper and lower FONLL bounds to obtain the theoretical uncertainties.

Figure 5.3 shows the calculated value of the charm production cross section $d\sigma_{c\bar{c}}/dy$ at $\langle y \rangle = 1.65$, together with the results from FONLL calculations, where the solid circle refers to $\langle y \rangle = -1.65$ and with a symmetrical point at $\langle y \rangle = 1.65$.

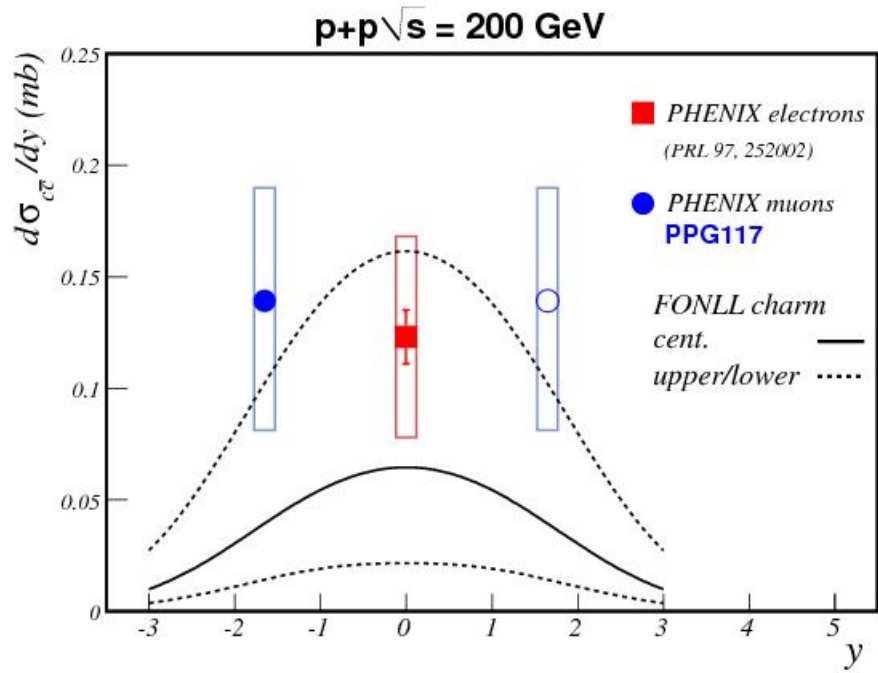


Figure 5.3: The rapidity distribution for the charm production cross section in p+p collisions through semi-leptonic decay into the electrons (square) and muons (circles) [37].

5.3 R_{AA} Measurements

Measurements of the nuclear modification factor for single muons produced in heavy flavor decay have been performed for three different centralities and extracted for each muon arm separately. In order to reduce the systematic uncertainties Equation 5.3 is used to calculate the final R_{AA} :

$$R_{AA}^i = \frac{1}{\langle N_{coll}^{CuCu} \rangle} \cdot \left(\frac{dN_{CuCu}}{dN_{p+p}} \right)^i, \quad (5.3)$$

where index i represents the package for the p+p and Cu+Cu background hadron cocktail calculation with the same set of physics assumptions. The methodology of calculation of R_{AA} is further described in Appendix A. Figures 5.4, 5.5, and 5.6 present the p_T distributions of the nuclear modification factor for production of single muons produced in heavy flavor decay for three different centrality ranges: 0-20%, 20-40%, and 40-94%, respectively. From those figures, we clearly observe that there is a significant suppression for the most central collisions for muons produced in heavy flavor decay.

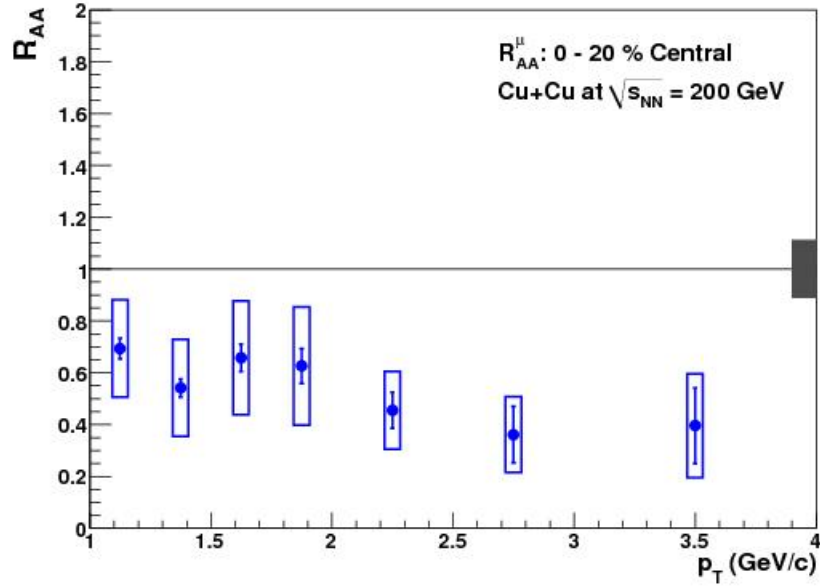


Figure 5.4: The transverse momentum distribution of the nuclear modification factor for single muons in Cu+Cu collisions for 0-20% centrality [37].

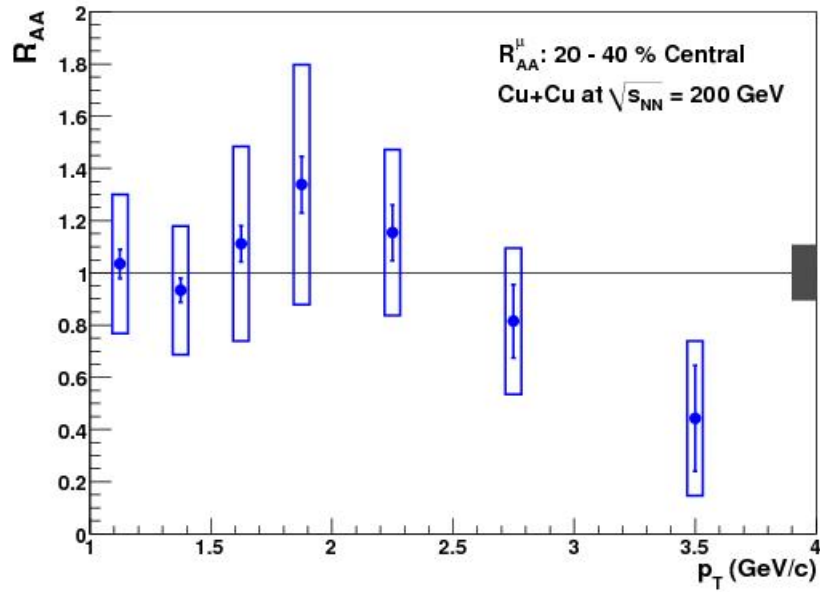


Figure 5.5: The transverse momentum distribution of the nuclear modification factor for single muons in Cu+Cu collisions for 20-40% centrality [37].

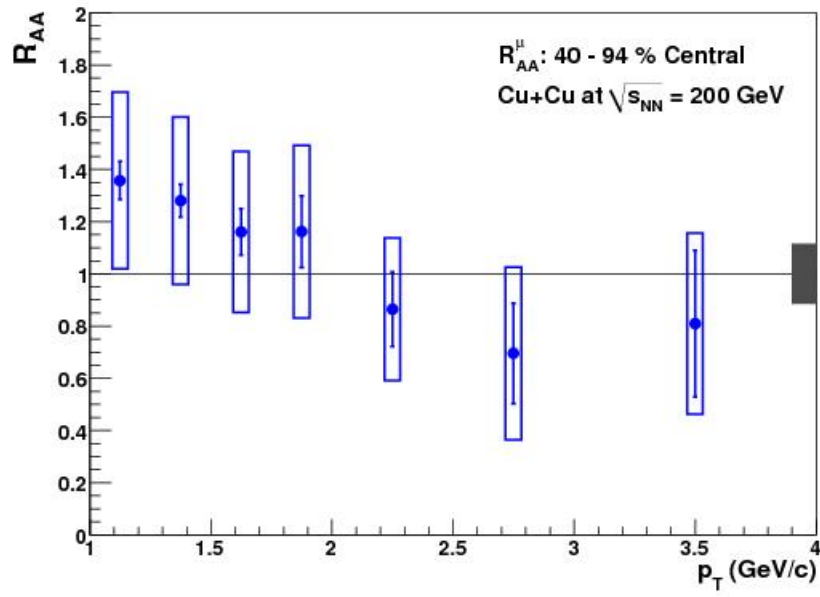


Figure 5.6: The transverse momentum distribution of the nuclear modification factor for single muons in Cu+Cu collisions for 40-94% centrality [37].

Chapter 6

Conclusions

The main goal of this thesis is to describe the measurement of the nuclear modification factor in Cu+Cu collisions at $\sqrt{s_{NN}} = 200$ GeV for the production of heavy flavor at forward rapidity. The nuclear modification factor has been measured near $|y| \approx 1.65$.

6.1 Overview

The achievements and advancements of the analysis described in this thesis include:

- The measurement of the transverse momentum distribution and centrality dependence of the nuclear modification factor for heavy flavor muons at $\sqrt{s_{NN}} = 200$ GeV for Cu+Cu collisions at forward rapidity. The nuclear modification factor has been measured for three different centrality intervals.
- The measurements show very strong suppression of heavy flavor production for the most central collisions.

- The first published measurements of the production of open heavy flavor mesons at forward rapidity in heavy ion collisions.
- The measurement of the transverse momentum distribution of the invariant yield of muons from open heavy flavor decay for all intervals of centrality in Cu+Cu collisions.
- The measurement of the transverse momentum distribution near $|y| = \pm 1.65$ of the differential cross section for muons from open heavy flavor decay in p+p collisions and estimation of the total charm production cross section.
- The developments presented in this thesis represent enhancements beyond two recent UTK PhD theses ([6] and [15]) with an improved joint analysis in order to achieve optimal cancellation of systematic uncertainties. These enhancements include significant reduction of systematic errors.
- Using the method described in Appendix A, reduced systematic uncertainties for R_{AA} have been achieved relative to PHENIX preliminary analysis.

6.2 Discussion

The main goal of this thesis is to study open heavy flavor production. In order to test previous theoretical predictions, the p_T and centrality dependence of the nuclear modification factor in Cu+Cu collisions have been measured. Another important result is the differential cross section for muons decaying from open heavy flavor in p+p collisions. This has been integrated in order to obtain the measured charm production cross section for p+p collisions at $\sqrt{s_{NN}} = 200$ GeV. Another achievement of the analysis are the measurements of the single muon spectra in Cu+Cu collisions since those represent the first measurements of the p_T spectra of invariant yields of open heavy flavor production in symmetric heavy ion collisions at forward rapidity.

The nuclear modification factor measurements for Cu+Cu central collisions show the yields are suppressed compared with p+p scaled collisions. There is indeed large suppression for Cu+Cu collisions at forward rapidity. Key techniques for the single muon signal extraction were developed and implemented by former UTK graduate student Donald Hornback [15]. Estimating the hadron background via the hadron cocktail improved measurements significantly. For Cu+Cu central collisions, high multiplicity is observed. Because of the high multiplicity environment the background simulations were embedded in real Cu+Cu events.

6.3 Comparisons

The measurements presented for the R_{AA} for 0-20% centrality agree very well with theoretical predictions using modified energy loss mechanisms [38]. There are few theoretical predictions for the semi-leptonic muon distributions due to charm decay in heavy ion collisions. As demonstrated in Appendix B, it is critical to have a prediction for the muon (not charm) transverse momentum distribution. Figure 6.1 shows good agreement between recent theoretical predictions and our result for 0-20% centrality.

6.4 Future plans

The joint analysis described in this thesis leaves room for future important measurements. For PHENIX Run 11, the high resolution silicon vertex detector (VTX) has been installed which will perform measurements of the charm and bottom production cross sections with less background, smaller systematic uncertainties, and extended range of p_T . The results of our analyses should help interpret measurements of J/ψ suppression in heavy ion collisions. Also, single electrons will continue to be used to study heavy flavor suppression.

The listed future measurements will certainly enrich our understanding of the in-medium energy loss mechanisms in hot dense partonic matter, as well as understanding of QCD matter at extremes of energy and density.

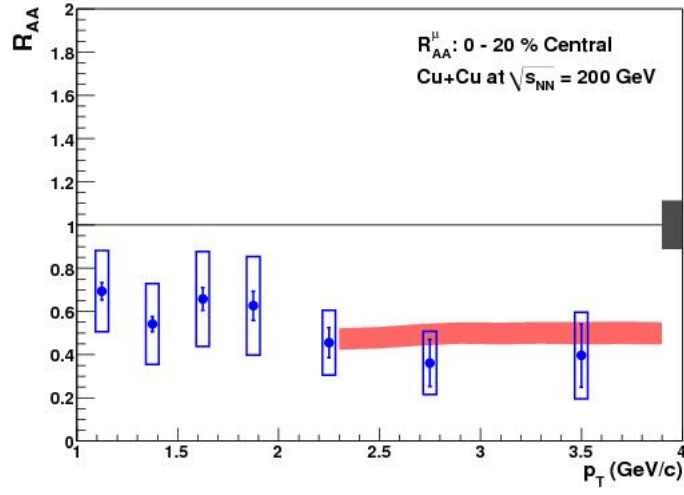


Figure 6.1: Transverse momentum distribution of the nuclear modification factor for single muon production from open heavy flavor decay in Cu+Cu collisions for 0-20% centrality [37] compared to a recent theoretical prediction [38].

Bibliography

- [1] Michael E. Peskin and Daniel V. Schroeder. *Quantum Field Theory*. Addison-Wesley, 1995.
- [2] Cheuk-Yin Wong. *Introduction to High-Energy Heavy-Ion Collisions*. World Scientific, 1994.
- [3] D. J. Gross and F. Wilczek. *Phys. Rev. Lett.*, **30**:1343–6, 1973.
- [4] H. D. Politzer. *Phys. Rev. Lett.*, **30**:1346–9, 1973.
- [5] E. V. Shuryak. *Phys. Rept.*, **61**, 1980.
- [6] Irakli Garishvili. *Open heavy flavor measurement at forward angles for Cu+Cu collisions at center of mass NN collision energy 200 GeV*. PhD thesis, University of Tennessee, 2009.
- [7] J. D. Bjorken. *Phys. Rev.*, **D27**:140, 1983.
- [8] K. Adcox et al. *Nucl.Phys.*, **A757**:184–283, 2005.
- [9] M. L. Miller, K. Reygens, Stephen J. Sanders, and P. Steinberg. *Ann.Rev.Nucl.Part.Sci.*, **57**:205–243, 2007.
- [10] S. S. Adler et al. *Phys. Rev. Lett.*, **91**:172301, 2003.
- [11] J. Adams et al. *Phys. Rev. Lett.*, **91**:172304, 2003.
- [12] E. Eichten, K. Gottfried, T. Kinoshita, K. D. Lane, and T. M. Yan. *Phys. Rev.*, **D21**:203, 1980.
- [13] H. Satz. *Rep. Prog. Phys.*, **63**:1511–1574, 2000.
- [14] M. C. Abreu et al. *Phys. Lett.*, **B477**:28–36, 2000.
- [15] Donald Hornback. *A measurement of open charm using single muons at forward angles for p+p collisions at center of mass energy 200 GeV*. PhD thesis, University of Tennessee, 2008.
- [16] J. C. Collins, D. E. Soper, and G. Sterman. *Nucl. Phys.*, **B263**:37–60, 1986.
- [17] C. Lourenço and H. K. Wöhri. *Phys. Rep.*, **433**:127–180, 2006.
- [18] C. Peterson, D. Schlatter, I. Schmitt, and P. M. Zerwas. *Phys. Rev.*, **D27**:105, 1983.

- [19] Bo Andersson, G. Gustafson, Ingelman G., and T. Sjostrand. *Phys. Rept.*, **97**:31, 1983.
- [20] D. Acosta et al. *Phys. Rev. Lett.*, **91**:241804, 2003.
- [21] Frederic J. Gilman and Jr. Robert. L. Singleton. *Phys. Rev.*, **D41**:142, 1989.
- [22] Jeffrey D. Richman and Patricia R. Burchat. *Rev. of Mod. Phys.*, **67**:893, 1995.
- [23] J. Y. et al Ge. *Phys. Rev.*, **D79**:052010, 2009.
- [24] M. Cacciari, P. Nason, and R. Vogt. *Phys. Rev. Lett.*, **98**:122001, 2005.
- [25] M. Cacciari and M. Greco. *Nucl. Phys.*, **B421**:530–544, 1994.
- [26] E. Braaten et al. *Phys. Rev.*, **D 51**:4119, 1995.
- [27] V. Kartvelishvili et al. *Phys. Lett.*, **B 78**:615, 1978.
- [28] B. Aubert et al. *Phys. Rev.*, **D 69**:111104, 2004.
- [29] A.H. Mahmood et al. *Phys. Rev.*, **D 70**:032003, 2004.
- [30] C. Amsler et al. Particle data group. *Phys. Lett.*, **B667**:1, 2008.
- [31] K. Adcox et al. *Nucl. Instr. and Meth. A*, **499**:469–479, 2003.
- [32] S. H. Aronson et al. *Nucl. Instr. and Meth. A*, **499**:593–602, 2003.
- [33] Jason Newby. *J/ψ production in Au+Au collisions at $\sqrt{s_{NN}} = 200$ GeV*. PhD thesis, 2003.
- [34] R. Brun. Geant 3.21 detector description and simulation tool. *CERN Program Library Long Write-up W5013*, 1994.
- [35] V. Ryabov for the PHENIX Collaboration. *arXiv:nucl-ex/0702046*, 2007.
- [36] A. Adare et al. 2010.
- [37] PHENIX collaboration. *To be submitted*, 2011.
- [38] A. Adil and I. Vitev. *Phys. Lett.*, **B649**:139, 2007.

Appendices

Appendix A

Weighted Sample Mean

The use of multiple background simulations, referred to as “hadron packages” have previously been discussed in [6] and [15]. These packages are a result of the modification of the internal GEANT3 hadron code cross sections (known as FLUKA and GHEISHA). Modification of these cross sections improves the match of data to simulation for gap 3 stopped hadrons and gap 4 inclusive muon candidates. The hadron package simulations are used to estimate backgrounds that are statistically subtracted to achieve a single muon yield. The procedure for mathematically combining the results from multiple simulation packages as well as how to propagate the systematic errors due to the hadron packages are outlined in the following 7 steps and represent how the final results are calculated. These steps describe how the p+p spectrum is calculated as well as the Cu+Cu R_{AA} . Subtle differences in the R_{AA} calculation are explicitly noted in each step.

A.1 R_{AA} Calculation Steps

Step 1 For each p_T bin i , hadronic cross section package j , and package tuning k , calculate the p+p cross section (or Cu+Cu R_{AA}) $Q_{i,j,k}$ where

- $k=1$ represents an overall optimal tuning for gaps 2, 3, and 4,
- $k=2$ represents tuning to reproduce the Gap 2 yield,
- $k=3$ represents tuning to reproduce the Gap 3 yield,
- $k=4$ represents tuning to reproduce the Gap 4 slopes.

The tuning $k=1$ is used for the central value.

Step 2 The package mismatch contribution to the error on the measurement Q is estimated by the sample standard deviation of the 4 particular different tunings

$$\sigma_{PackMismatch,i,j}^2 = \frac{\sum_{k=1}^4 Q_{i,j,k}^2}{4} - \left(\frac{\sum_{k=1}^4 Q_{i,j,k}}{4} \right)^2 = \frac{1}{4} \sum_{k=1}^4 \left(Q_{i,j,k} - \langle Q_{i,j,k} \rangle \right)^2 \quad (\text{A.1})$$

Step 3 For each p_T bin and package, compute the associated error $\sigma_{i,j}$ which includes all sources of error for the given package including the package mismatch uncertainty computed in Step 2. For p+p, uncertainties are propagated for the differential cross section (not yield) so the BBC uncertainties, $\sigma_{\sigma_{BBC}}$, are included in the full calculation. RAA is calculated using p+p and Cu+Cu yields so the BBC error term is not included.

The acceptance and efficiency uncertainty, $\sigma_{A\epsilon}$, is formed from four components: MuTR station data/MC comparisons (8%), MuID Gap 4 efficiency uncertainty (4.5%), run to run variation (2%), uncertainty in the J/ψ mass peak (1.5%). These four components added in quadrature amount to 9.5%. $\sigma_{SystPack}$ is the North/South arm common uncertainty associated with the hadron cocktail simulations. It is comprised of two 10% errors added in quadrature (which

amounts to 14.14%). The two components are uncertainty on the cocktail input distributions and the Gap 3 to Gap 4 efficiency matching error determined from simulations.

The full list of uncertainties are then given by the following:

$$\sigma_{i,j}^2 = \sigma_{StatData,i}^2 + \sigma_{StatPack,i,j}^2 + \sigma_{SystPack,i,j}^2 + \sigma_{PackMismatch,i,j}^2 + \sigma_{A\epsilon,i,j}^2 \quad (\text{A.2})$$

Note that $\sigma_{SystPack,i,j}$ is the same (common) for all j and is multiplied by the Background/Signal ratio. In the case of R_{AA} , the $\sigma_{A\epsilon,i}$ error cancels and is not included.

Step 4 Using $\sigma_{i,j}^2$ from Step 3, for each p_T bin compute the weighted sample mean of Q for the different packages:

$$\langle Q_i \rangle = \sum_{j=1}^5 W_{i,j} Q_{i,j,k=1} \quad (\text{A.3})$$

where

$$w_{i,j} \equiv \frac{\frac{1}{\sigma_{i,j}^2}}{\sum_{j=1}^5 \frac{1}{\sigma_{i,j}^2}} \quad (\text{A.4})$$

Step 5 The total error on the final measurement is the variance of the weighted sample mean:

$$Var(\langle Q_i \rangle) = \sum_{j=1}^5 W_{i,j}^2 Var(Q_{i,j,k=1}) + 2 \sum_{j < m}^5 w_{i,j} w_{i,m} Cov(Q_{i,j,k=1}, Q_{i,m,k=1}) \quad (\text{A.5})$$

In our case and using $\sigma_{i,j}$ defined in Step 3, this becomes:

$$Var(\langle Q_i \rangle) = \sum_{j=1}^5 w_{i,j}^2 \sigma_{i,j}^2 + 2 \sum_{j < m}^5 w_{i,j} w_{i,m} \sigma_{common,i}^2 \quad (\text{A.6})$$

where

$$\sigma_{common,i}^2 \equiv \sigma_{i,j}^2 - \sigma_{PackMismatch,i,j}^2 \quad (\text{A.7})$$

or

$$\sigma_{common,i}^2 = \sigma_{StatData}^2 + \sigma_{StatPack,i,j}^2 + \sigma_{SystPack,i,j}^2 + \sigma_{A\epsilon,i,j}^2 \quad (\text{A.8})$$

Step 6 Defining $\sigma_{StatCombined,i}$ error as the quadratic sum of the statistical errors of data and simulation, the final measurement **per arm** for a given p_T bin is:

$$\langle Q_i \rangle \pm \sigma_{StatCombined,i} \pm \sigma_{Model,i} \pm \sigma_{A\epsilon,i} \pm \sigma_{\sigma BBC,i} \quad (\text{A.9})$$

where $\sigma_{Model,i}$ is defined as:

$$\sigma_{Model,i} \equiv (Var(\langle Q_i \rangle) - \sigma_{StatCombined,i}^2 - \sigma_{\sigma_{A\epsilon,i,j}}^2)^{0.5} \quad (\text{A.10})$$

The BBC uncertainty $\sigma_{\sigma BBC}$ is taken from the uncertainty on $\sigma_{\sigma BBC}^{pp}$ and has a value of 9.6%. For the case of R_{AA} , both $\sigma_{\sigma BBC,i}$ and $\sigma_{A\epsilon,i}$ are not included.

Step 7 The independent North and South Measurements are combined and represented by Q , where j is the arm index and i is the p_T index:

$$\langle Q_i \rangle = \sum_{j=1}^2 w_{i,j} Q_{i,j} \quad (\text{A.11})$$

and the weights, as before, are calculated by:

$$w_{i,j} \equiv \frac{\frac{1}{\sigma_{i,j}^2}}{\sum_{j=1}^2 \frac{1}{\sigma_{i,j}^2}} \quad (\text{A.12})$$

An arm mismatch error is assigned so that the total uncertainty for the final combined arm measurement:

$$\sigma_i^2 = \sigma_{StatCombined,i}^2 + \sigma_{Model,i}^2 + \sigma_{A\epsilon,i,j}^2 + \sigma_{ArmMismatch,i}^2 \quad (\text{A.13})$$

where the arm mismatch error is calculated in step 2:

$$\sigma_{ArmMismatch,i}^2 = \frac{\sum_{j=1}^2 Q_{i,j}^2}{2} - \left(\frac{\sum_{j=1}^2 Q_{i,j}}{2} \right)^2 \quad (\text{A.14})$$

For the case of R_{AA} and $\sigma_{A\epsilon,i}$ cancels and is not included. For p+p, inclusion of $\sigma_{\sigma BBC,i}$ is postponed at this point and is added in quadrature in the final step. The final combined arm σ_i^2 is calculated according to the following (where again j is the arm index and i is the p_T index):

$$Var(\langle Q_i \rangle) = \sum_{j=1}^2 W_{i,j}^2 \sigma_{i,j}^2 + 2 \sum_{j < m}^5 w_{i,j} w_{i,m} \sigma_{armcommon,i}^2 \quad (\text{A.15})$$

where

$$\sigma_{armcommon,i}^2 = \sigma_{A\epsilon,i}^2 + \sigma_{SystPack,i}^2 \quad (\text{A.16})$$

The uncertainty $\sigma_{armcommon,i}^2$ is asserted to be the contribution to the covariant term (arm correlated) and arises from an uncertainty common to both arms. For the case of R_{AA} , $\sigma_{A\epsilon,i}$ is not included.

The final statement of the combined systematic uncertainty bands for Q_i for plotting purposes is (for the case of R_{AA} , $\sigma_{\sigma BBC,i}$ is not included):

$$\sigma_{FinalError,i}^2 = (Var(\langle Q_i \rangle) - \sigma_{StatCombined,i}^2) \pm \sigma_{\sigma BBC,i}^2 \quad (A.17)$$

A.2 Final Step

The final statement of the measurement and uncertainties is then:

$$\langle Q_i \rangle \pm \sigma_{FinalError,i} \pm \sigma_{StatCombined,i} \quad (A.18)$$

where again for the case of R_{AA} , $\sigma_{\sigma BBC,i}$ is not included in the systematic uncertainty bands represented by $\sigma_{FinalError,i}$. $\langle Q_i \rangle$ is the weighted mean of the North and South arm measurements. $\sigma_{FinalError,i}$ is drawn as the one-sigma systematic uncertainty bands and $\sigma_{StatCombined,i}^2$ is drawn as the point-to-point uncorrelated statistical error bars.

A.3 Simple Example

Consider the weighted mean and weighted sample variance for a set of measurements

$$\mu = \frac{\sum_i \frac{x_i}{\sigma_i^2}}{\sum_i \frac{1}{\sigma_i^2}} \quad (A.19)$$

$$\sigma_\mu^2 = \frac{\sum_i \left(\frac{x_i - \mu}{\sigma_i} \right)^2}{\sum_i \left(\frac{1}{\sigma_i} \right)^2} \quad (A.20)$$

For the case of two measurements of 20 ± 1 and 40 ± 1 , the weighted results are:

$$\mu = \frac{\frac{20}{1^2} + \frac{40}{1^2}}{\frac{1}{1^2} + \frac{1}{1^2}} = 30 \quad (\text{A.21})$$

$$\sigma_\mu^2 = \left[\frac{\left(\frac{20-30}{1}\right)^2 + \left(\frac{40-30}{1}\right)^2}{\left(\frac{1}{1^2}\right)^2 + \left(\frac{1}{1^2}\right)^2} \right]^{0.5} = 10 \quad (\text{A.22})$$

In this case, the results are the same as ROOT TH1::GetMean and GetRMS for the related distribution. Note that the weighted sample variance is not $\sigma = \sqrt{\sigma_1^2 + \sigma_2^2} = \sqrt{1+1} = 1.41$.

Next, for the related case of 20 ± 1 and 40 ± 10 , the weighted mean (which is very different from GetMean for the related distribution) and weighted sample variance are:

$$\mu = \frac{\frac{20}{1^2} + \frac{40}{10^2}}{\frac{1}{1^2} + \frac{1}{10^2}} = 20.2 \quad (\text{A.23})$$

$$\sigma_\mu^2 = \left[\frac{\left(\frac{20-20.2}{1}\right)^2 + \left(\frac{40-20.2}{10}\right)^2}{\left(\frac{1}{1^2}\right)^2 + \left(\frac{1}{10^2}\right)^2} \right]^{0.5} = 10 \quad (\text{A.24})$$

Appendix B

Charm Meson Decay Kinematics

In our analysis, we study the production of D mesons in p+p collisions which later decay semi-leptonically into muons and other particles depending on whether it is a three-body or more decay. Muons produced via semi-leptonic decay have great importance in our analysis since we use them to tag open heavy flavor.

In this Appendix we present kinematic studies of the semi-leptonic decay of D mesons into muons performed using PYTHIA generator. About 1000000 p+p collisions have been generated.

Figure B.1 (upper panel) compares the total momentum of D mesons and resulting muons. Figure B.1 (lower panel) compares transverse momenta.

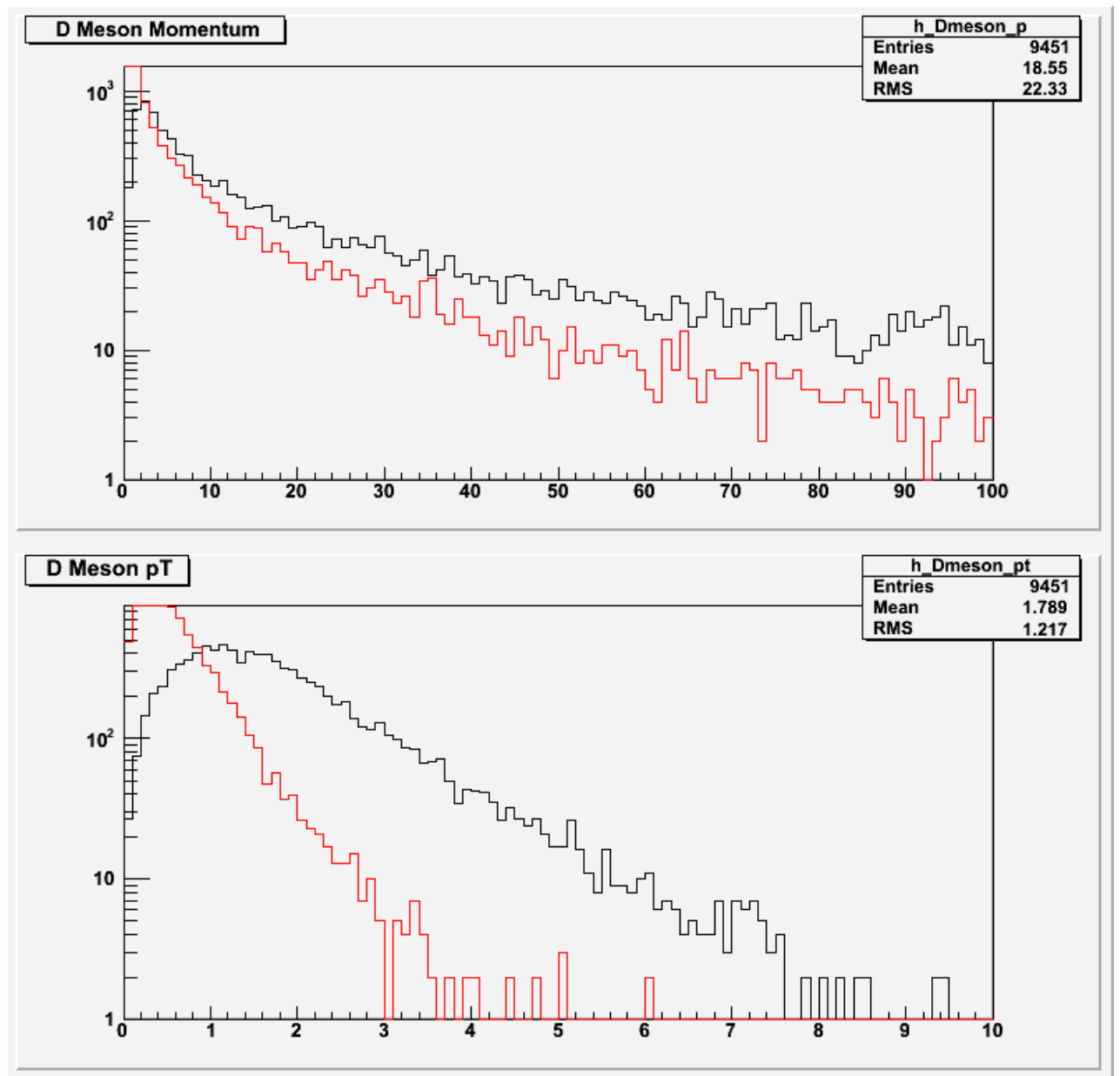


Figure B.1: Upper plot illustrates the distribution of total momentum of D meson (black line) and muon (red line), lower plot illustrates the distribution of transverse momentum of D meson (black line) and muon (red line).

Figure B.2 compares the pseudorapidity (upper panel) and rapidity (lower panel) of mother and daughter particles in heavy flavor semi-leptonic decay.

In conclusion, we see that it is not possible to clearly obtain the parent D meson (or c quark) momentum accurately by using single leptons. Instead, a theoretical prediction of the differential suppression of D mesons (or c quarks) must be followed by a simple (after-burner) prediction of the (suppressed) single lepton production as a function of transverse momentum.

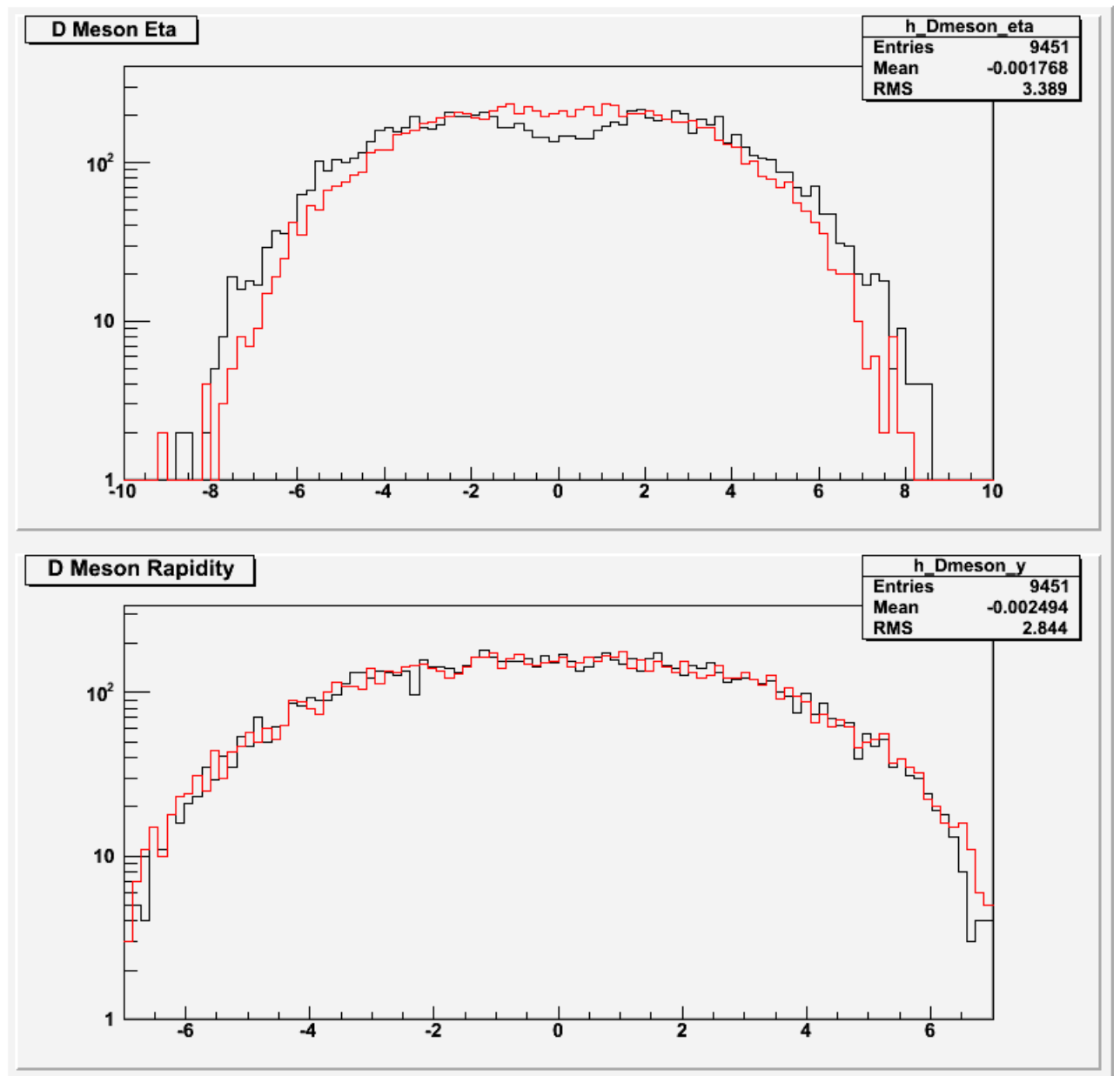


Figure B.2: Upper panel shows the distribution of pseudo rapidity of D mesons (black line) and muons from their semi-leptonic decay (red line). Lower panel shows the distribution of rapidity of D mesons (black line) and daughter muons (red line).

Vita

Archil Garishvili was born on March 27, 1981 in Tbilisi, Georgia (a former soviet republic). In 1998, after graduating from A. Razmadze Physical and Mathematical Gymnasium #7 of Tbilisi, he enrolled in the Department of Physics of Tbilisi State University (TSU). He graduated in 2002 with a B.Sc. degree. He attended the University of Tennessee from June 2009 through December 2011. He graduated with a Masters of Science in December 2011.